Institute of Paper Science and Technology
Atlanta, Georgia

IPST TECHNICAL PAPER SERIES

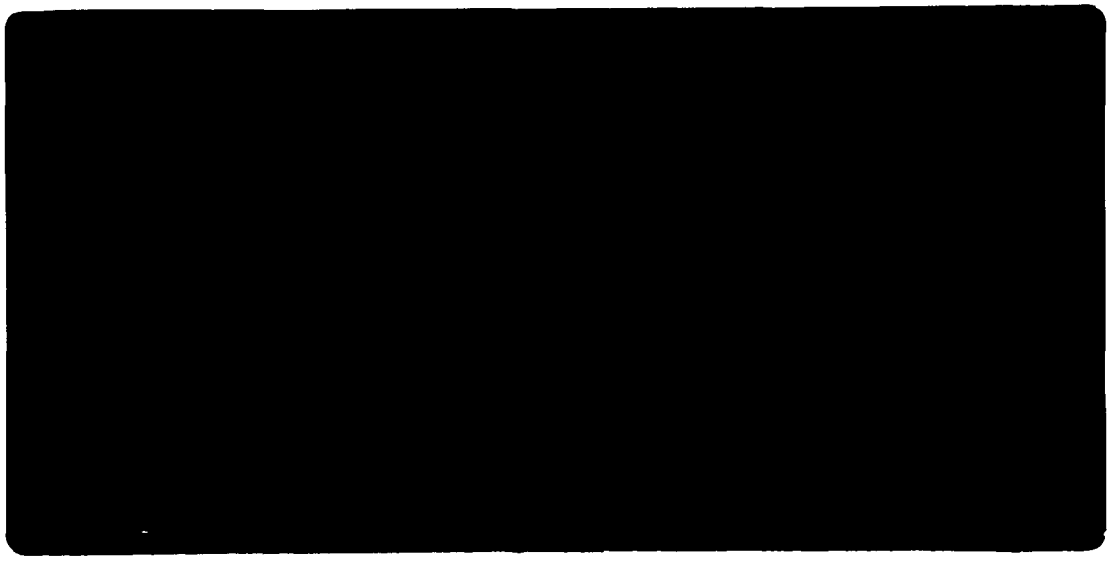

NUMBER 407

EFFECTS OF CD PRESSURE VARIATIONS ON COAT-WEIGHT NONUNIFORMITIES

H. MIURA AND C.K. AIDUN

NOVEMBER, 1991

Effects of CD Pressure Variations on Coat-Weight Nonuniformities

S. Banerjee

Submitted for publication in
AIChE Journal

ABSTRACT

In this paper, we computationally investigate the relationship between pressure fluctuations upstream the blade nip and nonuniformities of the wet-film thickness.

The motivation for this study comes from earlier investigation of the flow in the pond of short-dwell coaters. Although these coaters are very popular in surface treatment of paper, the trend toward increasing coating speed is hindered by the difficulty in maintaining uniform coat-weight profile in the cross-machine direction (CD). Past studies suggest that three-dimensional hydrodynamic instability inside the short-dwell pond, where the flow becomes unsteady and nonuniform as coating speed increases, is a major contributor to coat-weight nonuniformities in the CD.

In this and other blade coating systems, disturbances upstream of the blade generate a nonuniform wavy coating color layer entering the blade nip with the moving web. Consequently, the normal stress upstream the blade, which affects the pressure-driven flow, becomes nonuniform in the CD, and subsequently, generates coat-weight nonuniformities. The effect and significance of the pressure fluctuations upstream of the blade on coat-weight nonuniformities is the central issue addressed in this study.

EFFECTS OF CD PRESSURE VARIATIONS ON COAT-WEIGHT NONUNIFORMITIES

Hiroshi Miura and Cyrus K. Aidun*

Engineering Division

Institute of Paper Science and Technology

Atlanta, Georgia 30318

KEYWORDS

Blade Coating, Three-Dimensional Flow, Pressure Fluctuations, Coat-Weight Nonuniformities.

INTRODUCTION

The objective of coating processes is to apply a coating color to a moving web to produce a smooth and uniform surface for good printability. Increasing demand for light-weight coated paper has generated the trend toward increasing machine speed while reducing coat weight in blade coaters. Meeting this trend, short dwell-time coaters (SDC) have gained popularity over the past 10 years. In SDC the flexible blade acts both as a boundary of the coating color reservoir (SDC pond) and as a metering unit (Fig. 1). SDC have advantages of compactness, low color penetration, long blade life, and less sheet break due to low blade loading. But movement toward

*Correspondence concerning this article should be addressed to C.K. Aidun, Institute of Paper Science and Technology, 575 14th Street, N.W., Atlanta, GA, 30318.

H. Miura is currently a Research Engineer with Mitsubishi Corp., 5007 Itozaki-cho, Mihara, Hiroshima Pref., 729-03, Japan.

further increase of coating speed with SDC has been hindered by difficulty in maintaining uniform coat-weight profile in the CD. In its extreme case, an uneven coat-weight profile appears as a patterned surface characterized by streaks of 1 to 3 cm wide running along the machine direction (MD). We should note that this length scale (~ 1 cm) is orders of magnitude larger than the blade gap (~ 30-50 μm) and that these streaks have, in general, less coat weight than the rest of the coated surface. The streaks are estimated to have 15 to 50 percent deficit in coat-weight relative to the rest of the coated surface. This is in contrast to streaks caused by a solid particle blocking the blade gap, or skip coating, where the streaks essentially have no coating. Wet streaks occur when the machine speed increases above a critical limit for a given coating color viscosity. Pilot coater trials (Triantafillopoulos and Aidun, 1990 and Li, 1990) show that this limiting speed decreases by increasing the percentage solids, and consequently, the low-shear viscosity of the coating color.

Experiments with Newtonian fluids and a through-flow lid-driven cavity simulating the pond of a short-dwell coater (Aidun et al., 1991a and Benson and Aidun, 1991) revealed the sequence of transitions from steady state (SS) to time-periodic (TP), and eventually, a state with more than one fundamental frequency (see Fig. 2) referred to, from now on, as the "unsteady state." This state seems to follow a quasi-periodic state (QP) at Re ~ 1000 and is characterized by a broad band of frequencies.** The mushroom-shape structures which appear at the unsteady state (Fig. 2d) could be an initial state of Görtler-like vortices observed by Koseff and Street (5)

**The measurements by Benson and Aidun (1991) suggest a SS→TP→QP→chaotic sequence of transitions. Rigorous stability analysis is required to map the transitions more accurately and to establish the sequence of instabilities to unsteady nonperiodic (chaotic) flow.

state (Fig. 2d) could be an initial state of Görtler-like vortices observed by Koseff and Street (5) in a confined lid-driven cavity flow at Re = 3200. It is important to note that the length scale of the mushroom-shape vortices (Fig. 2d) is the same as the width of the wet streaks discussed above. Also, the dynamical characteristics of the streaks correspond to the rapid motion of these structures in the pond. Based on these observations, we conclude that these structures are an important factor in generating the streaks.

There are a number of ways that flow instability in the pond upstream of the blade can cause film thickness nonuniformities. These are summarized in Fig. 3. Air entrainment proposed by Aidun (1989) is one of the prime candidates. The recent pilot coater experiments by Li and Burns (1991) show a decrease in the streaks as the air accumulated inside the pond is removed. The sequence of events leading to air entrainment in the form of small bubbles from a dynamic contact line is revealed by Veverka and Aidun (1991) and Aidun et al. (1991b). We emphasize that this mode of air entrainment in the form of air bubbles entering and accumulating inside the pond occurs at machine speeds lower than the speed resulting in skip coating.

This paper focuses on the second mechanism represented in Fig. 3. A three-dimensional (3-D) flow upstream of the blade results in some variations in the static pressure at the blade gap entrance. Since a portion of the mass transfer into the blade gap is pressure driven, the variation in static pressure could result in coat-weight variations. Here, we examine the importance of temporal as well as spatial pressure variations in the cross-machine (spanwise) direction. This requires solution of the equations governing the transient 3-D flow at the blade. All of the previous computational analyses of blade coating assume no flow or variations in the third dimension. A two-dimensional (2-D) analysis can be extremely useful in terms of predicting an

average coat-weight and investigating the various blade coating features, such as substrate and blade deformation (Pranckh and Scriven, 1988, 1990), coating color penetration into the substrate (Chen and Scriven, 1989), and design of new coating application systems (Aidun, 1992). Conclusions made from 2-D computations without including a stability analysis, however, could be somewhat misleading. We now know that the solution of a steady, 2-D flow in the pond of a short-dwell coater represents a solution branch which is locally unstable to a TP state at Re > 900 (Aidun et al., 1991a). Therefore, the 2-D SS solutions reported in previous studies (Triantafillopoulos et al., 1988, 1989; Affes et al., 1990; and Conlisk and Foster, 1991) are unstable to infinitesimal disturbances and do not represent a physical flow at Reynolds number above 900.

Linear stability analysis of 2-D flows in slide coating (Christodoulou and Scriven, 1989) have proved to be quite effective. In this study, however, to investigate the magnitude of the meniscus nonuniformity in the spanwise direction due to pressure variations upstream of the blade gap, we have to solve the full transient 3-D flow equations. Including the third dimension in the analysis increases the computational cells by an order of magnitude. The added complexity of solving the strongly nonlinear interfacial conditions at the free surface, which now has two radii of curvatures, demands a careful setup of the domain and the boundary conditions for a most efficient, and therefore, tractable problem. Since the main objective in this study is to determine the significance of coat-weight variations caused by the pressure fluctuations upstream the blade, we consider a nonporous smooth substrate (e.g., the backing roll) and neglect the deformation of the substrate and the blade. This will isolate the effect of the third feature introduced by Fig. 3, that is, nonuniform deformation of the substrate and the blade gap opening.

This is a preliminary computational study in a continuing effort to analyze the various mechanisms of large- and small-scale coat-weight nonuniformities with blade coating systems.

COMPUTATIONAL TECHNIQUE

In contrast to confined flows where the boundaries are well-defined and fixed in time, free surface flow problems introduce an added complexity due to the a priori unknown location and shape of the interface. Numerical algorithms for free surface problems normally start from an initial condition and compute the shape of the interface according to the interfacial conditions. There are two fundamental categories of computational techniques for free surface flow calculations. One class requires that the interfaces coincide with the element or grid boundary, and therefore, the elements adjacent to the interface are forced to deform with the free surface. Finite element methods developed for free surface calculations fall within this class. This technique works well for free surface flows with small deformations. But for large deformations, the excessive deformation of the elements results in various problems including the technique's inability to converge. In this situation, it is necessary to use strategic continuation techniques and remeshing of the domain.

We have adopted a second class of computational techniques for free surface flows where the fluid is convected through fixed grids, and the free surface can deform, according to the interfacial conditions, independently of the grid system. This feature allows computation of flows with large deformation and discontinuous surfaces to be routine. The grids which are crossed by the liquid surface are partially full and have to be treated in a special manner. We use the volume-of-fluid (VOF) techniques (Torrey et al., 1987) where the VOF in the surface cells is

treated as an additional dependent function of position and time, F(x, t), governed by the convective equation

$$\frac{DF}{Dt} = u_n \tag{1}$$

where D/Dt is a material derivative, and u_n is the fluid velocity normal to the free surface. This equation follows from the kinematic condition requiring the free surface to be a streamline or a material surface in 3-D flow problems. The value of F can vary from 0, for an empty cell, to 1, for a full cell. This technique was used successfully in the past (Torrey et al., 1987) for calculation of free surface problems where the tangential and normal viscous stress conditions at the interface could be neglected. For problems where accurate computation of the free surface deformation is not required, such as the drainage of a tank, surface stress conditions can be neglected. In our application, however, we are interested in an accurate determination of the free surface shape, and therefore, must include the complete nonlinear surface conditions. We apply the full normal and tangential stress conditions given, respectively, by

$$\left[-p + 2\mu \frac{\partial u_n}{\partial n}\right]_A = \left[-p + 2\mu \frac{\partial u_n}{\partial n}\right]_B - \sigma\left(\frac{1}{R_1} + \frac{1}{R_2}\right) \tag{2}$$

and

$$\left[\mu\left(\frac{\partial u_n}{\partial t} + \frac{\partial u_t}{\partial n}\right)\right]_A = \left[\mu\left(\frac{\partial u_n}{\partial t} + \frac{\partial u_t}{\partial n}\right)\right]_B \tag{3}$$

Here, n and t are the normal and tangential directions with respect to the interface; σ is the surface tension; R_1 and R_2 are the radii of curvature. The brackets designated by subscripts A and B correspond to the phases, such as liquid and air, forming the interface. In coating applications, since the viscosity of coating fluid is orders of magnitude larger than the viscosity of air, we neglect the normal and tangential viscous stresses of phase B (air) in Eqs. (2) and (3).

The continuity and full momentum equations are solved using finite difference techniques based on SOLA (SOLution Algorithm) and the QUICK (Quadratic Upstream Interpolation for Convective Kinematics) methods. The SOLA method, which was originally formulated by Hirt et al. (1975), is a linear combination of first-order accurate upwind differences and second-order accurate centered differences. The QUICK method, originally proposed by Leonard (1978) for use of finite volume derivations, is a third-order accurate upwind differencing scheme which possesses the stability of first-order upwinding but is free of its second-order numerical diffusion. For a 2-D local (ξ,η) coordinate system, Leonard fitted a six-point quadratic interpolation surface with the form given by

$$\Phi = C_1 + C_2\xi + C_3\xi^2 + C_4\eta + C_5\eta^2 + C_6\xi\eta \tag{4}$$

and yielded the QUICK formula given by

$$\Phi = \frac{1}{2}(\Phi_L + \Phi_L) - \frac{1}{8}(\Phi_C - 2\Phi_L - \Phi_{LL}) + \frac{1}{24}(\Phi_{TL} - 2\Phi_L + \Phi_{BL}) \tag{5}$$

The last term on the right-hand side, which represents a small upstream-weighed transverse curvature effect, is reported to have negligible impact on the computed flow field (Freitas et al., 1985). This term is neglected in our computation, yielding a one-dimensional form of the interpolation where we lose a little accuracy but greatly simplify the computations.

A typical simulation in this study begins by specifying initial domain and applying an initial value for the velocities and pressure in the computational domain with the appropriate boundary conditions. The governing equations are then projected onto the discretized domain using finite difference approximations, and the results are written in terms of the velocity and pressure field at the current and next time steps, n and n+1, respectively, by

$$\upsilon^{n+1} = [\upsilon^n + \Delta\theta(-\upsilon^n \cdot \nabla\upsilon^n + g + \nu\nabla^2\upsilon^n)] - \frac{\Delta\theta}{\rho}\nabla Pn+1 \tag{6}$$

Substituting Eq. (6) into the continuity equation yields

$$\frac{\Delta\theta}{\rho}\nabla^2 P^{n+1} = \nabla \cdot [v^n + \Delta\theta(-v^n \cdot \nabla v^n + g + \nu\nabla^2 v^n)] \tag{7}$$

Eq. (7), Poisson equation for pressure, is solved for the pressure field at the next time step by the conjugate residual method. The resulting pressure field is then substituted into Eq. (6) to provide the new velocity field. This procedure is continued until the desired time step is reached.

The accuracy of the technique described above has been intensively examined in a recent study (McKibben and Aidun, 1991), using both confined and free surface flows, and solutions are compared with the results in the literature.

We apply this technique to solve the 3-D flow of a highly viscous coating fluid at the blade. The flow at the entrance side of the blade consists of a shear-driven (Couette-flow) and a pressure-driven (Poiseuille-flow) component (Pranckh and Scriven, 1988, 1990).

We use the web speed, W, and the blade gap, h, for the velocity and length scales. We use the convective time scale, h/W, and μW/h for the pressure scale. From here on all of the variables shall be considered as dimensionless unless otherwise stated.

The inlet velocity boundary condition at the blade gap (Fig. 4a) consists of Couette- and Poiseuille-flow components given by

$$w(x, y, t) = 1 - x + \frac{1}{2} \cdot \frac{dp}{dz} \cdot x(x - 1) \quad at \quad z=0 \tag{8}$$

where the pressure gradient, dp/dz, can be a function of spanwise position, y, and time, t. The problem considered here has two parameters, namely the Reynolds number, $R \equiv \rho Wh/\mu$ and the capillary number, $Ca \equiv \mu W/\sigma$.

Analysis of flow at the blade nip involves mathematical treatment of a deforming meniscus and a static contact point at the exit side tip of the blade. Local analysis of the flow near the static contact point (Michael, 1958) in a die-swell problem shows that the discontinuity in shear and stress results in a mathematical singularity in the continuum approximation. This results in pressure and velocity gradients increasing without bound as $r^{-1/2}$, where r is the distance from the static contact point. The contact angle at this point is a major factor influencing the shape of the meniscus. We treat this point in a special manner. The point is fixed at the sharp corner of the solid, and the contact angle is determined from the equations and the interfacial conditions. We have done a thorough examination of our technique for accuracy by solving the die-swell problem and comparing the results with the literature. The results are reported by McKibben and Aidun (1991).

2-D BASE CASE

We use a SS 2-D flow as an initial condition for the transient as well as the base case for the 3-D analyses. In the 2-D cases, the surface tension effects are neglected. The flow entering

the blade gap is assumed to be a parallel flow given by Eq. (8). The walls satisfy the no-slip boundary condition, and the boundary condition downstream of the blade exit is given by

$$\frac{\partial}{\partial z}(\cdot) = 0 \quad at \quad z = \zeta \tag{9}$$

where $(\cdot)$ represents any dependent variable, and ζ is the total length of the domain in the z-direction, as illustrated in Fig. 4b.

To examine the independence of the results from domain length and grid size, we compute a test case at R = 19.2 and the blade thickness, $\tau = 2.5$. The initial condition for this simulation is a linear velocity profile (no pressure gradient) under the blade, F = 1 for all the cells inside the blade gap, and F = 0 for all the other cells. This indicates that the flow has reached the static contact point (Fig. 4b) and is starting to form a meniscus upstream of the blade. The transient equations are solved from this initial condition, and the results asymptotically approach a SS condition. The problem is solved with the coarse as well as the fine grid system, illustrated in Figs. 5a and 5b.

The evolution of the free surface from time 0 to 25 is shown in Figs. 6a and 6b, corresponding to the coarse and the fine grids, respectively. The two free surface profiles at time 25 are compared in Fig. 7. Although the results are close to one another, the coarse grid shows a slight numerical instability near the static contact point. This problem is resolved by refining the gird in that region as shown by the surface curve computed with the fine grid system. The

final thickness of the film has to be equal to .5. The value for the film thickness obtained from the domain length 12.5 is .50025 at t = 25. Increasing the domain length and the final time, the film thickness computed becomes .50001 at t = 45 (see Fig. 8).

We have also examined the accuracy of the results by noting the velocity profile at the outlet boundary upstream of the domain. The flow far downstream has a constant velocity, u = 0, and w = 1.0. Table 1 shows the velocity profile of the film at various locations downstream of the blade. The flow becomes essentially unidirectional at z ~ 20.

TP PRESSURE FLUCTUATION

In addition to the wet streaks which are coat-weight nonuniformities in the spanwise direction, the film thickness can also develop a 2-D wavy profile due to temporal fluctuation upstream of the blade. In this section, we examine the effect of the time-dependent fluctuation of static pressure at the blade entrance on the film thickness.

We assume a sinusoidal pressure fluctuation given by

$$\frac{dp}{dz} = \langle \frac{dp}{dz} \rangle \left[1 + .5 \sin\left(\frac{2\pi t}{T} \right) \right] \quad , \quad 0 < t < 2T$$

$$\frac{dp}{dz} = \langle \frac{dp}{dz} \rangle \quad , \quad t > 2T \tag{10}$$

where $\langle \cdot \rangle$ indicates a time-averaged magnitude, and T is the period of fluctuation.

The inflow condition becomes time dependent according to Eq. (10), while the other boundary conditions remain unchanged. Three cases were executed corresponding to the Reynolds numbers of 12, 24, and 30. The blade gap was reduced to a more realistic value of 50 microns resulting in a dimensionless blade thickness, $\tau = 20$. For a typical color viscosity of .05 Pa·s, density of 1.2 g/cm^3, and a blade gap of .05 mm, the three cases presented in this section correspond to coating speeds of 10, 20, and 25 m/s, respectively. The dimensionless average pressure gradient is specified as $\langle dp/dt \rangle = -.5$. In dimensional form, this pressure gradient corresponds to -1×10^8, -2×10^8, and -2.5×10^8 (Pa/m) for the three coating speeds, respectively. These values fall within the operating range of high-speed coaters of interest to this study.

Fig. 9 represents the computational domain and the grid system. Note that the vertical direction is greatly scaled up in this and the following figures. The small roughness at the meniscus surface is due to the interpolation of the F values in adjacent cells.

Fig. 10 shows the film thickness at 0.2 msec for the three cases considered. The film thickness fluctuation is small, as expected. Note that integrating Eq. (8) shows that more than 91.7% of the mass flow rate through the blade gap is shear driven. Therefore, one could assume that a 50% fluctuation in the static pressure results in about ~ 4% film thickness variation. The film thickness variation from the average value plotted in Fig. 11 for each case shows a maximum of 1% thickness variation. This is much smaller than the value predicted from a simple linear analysis demonstrating the importance of the nonlinearities introduced by the meniscus which reduces the full impact of the pressure fluctuations. However, the results show that variations in thickness increase in the second cycle as the meniscus approaches a TP fluctuation.

PRESSURE GRADIENT VARIATION IN THE THIRD DIMENSION

The flow instability upstream of the blade results in pressure gradient variations in the spanwise (cross-machine) direction. The purpose of the 3-D computations, presented in this section, is to investigate the importance of the static pressure fluctuations on the film thickness nonuniformity. Depending on the type of flow instability, the wavelength of the pressure variation could vary from a millimeter to about a centimeter or more.

The effect of film thickness nonuniformities is most important in light-weight coating where the blade gap is about 30 μm. The dimensionless parameters and a typical dimensional value used for the 3-D computations are listed in Table 2. The Reynolds number and Capillary number fall within the range of actual operating conditions. Although coating fluids are usually shear thinning, here we assume a contact viscosity based on the typical value at high-shear rates in the order of 10^{-6} 1/s. The average value of the pressure gradient at the blade nip inlet is estimated from the finite element computations by Pranckh and Scriven (1988) which is currently the most complete analysis of 2-D blade coating.

The pressure fluctuation in the y-direction is approximated as a sinusoidal variation given by

$$\frac{dp}{dz} = \left|\frac{dp}{dz}\right| \left[1 + 0.5 \cos\left(\frac{n\pi y}{Y}\right)\right] \tag{11}$$

where $|\cdot|$ indicates spatial average in the y-direction, and Y is the pressure fluctuation wave-

length. The value of n could be 1 or 2, representing half-wave or full-wave fluctuations, respectively.*** The pressure is again allowed to vary by 50% in magnitude. All of the boundary conditions remain as before with the addition of symmetry plane conditions imposed at the side walls, such that

$$u = \frac{\partial v}{\partial x} = \frac{\partial w}{\partial x} = \frac{\partial p}{\partial x} = 0 \quad at \quad y = \pm Y/2 \tag{12}$$

In this series of computations, the main parameter is the spanlength, Y, which is varied from 33.3 to 400 corresponding to a dimensional length of 1 mm to 1.2 cm. All of the 3-D simulations start from a 2-D base case solution shown in Fig. 12 where the grid system and the free surface are plotted. The final film thickness, calculated from integrating Eq. (8), is given by

0.5	+	.12	= 0.62
Couette-flow contribution		Poiseuille-flow contribution	Total

***In our analysis, we have considered cases with a full-wave of pressure fluctuation to examine any remote possibilities of symmetry breaking instabilities. None of the cases considered in this study, however, became unsymmetric.

The film thickness predicted computationally is 0.6206 which is accurate enough for all practical purposes. The pressure adjacent to the substrate (i.e., at $\chi = 0$) is plotted in Fig. 13. Results show a negative pressure at the blade tip which agrees with the results from parallel blade setting computed by Pranckh and Scriven (1988).

We shall discuss the results for several 3-D cases as summarized in Table 3.

The pressure fluctuation wavelength, Y, ranges from 33.3 (1 mm) to 200 (6 mm). The last two Cases, 9 and 10, are obtained with a half-wave fluctuation and a symmetry plane to simulate a span that is 400 (1.2 cm) long. None of the Cases with full-waves showed any sign of symmetry breaking instability. Based on this, we conclude that the flow remains symmetric with respect to the y = 0 plane. We used the higher order accurate QUICK finite differencing scheme for all Cases except 6, 7, and 8 where we used SOLA for comparison purposes. Also, to show that the results are independent of the grid size in the y-direction, we increased the number of grids by a factor of two and compared the results. The results for Cases 2, 3, 5, and 10 are presented in Figs. 14 to 17, respectively. We emphasize that the only physical parameter varied is the spanwise wavelength of the pressure fluctuation. The effect of grid refinement from 20 to 10 cells in the y-direction on the film thickness and the pressure profiles is presented by Figs. 18 and 19, respectively. Also, the film thickness profile computed with the higher order QUICK differencing scheme is compared in Fig. 20 with results from Case 7 using SOLA.

Figs. 18, 19, and 20 show that although increasing the grid size and the order of differencing provides more accurate results for the meniscus profile near the blade exit tip, these changes have virtually no effect on the overall shape of the meniscus, as well as, the film

thickness profile further downstream and the pressure profile under the blade. It demonstrates that the overall feature of our computational results are not influenced by numerical artifacts.

Comparing the film thickness profiles for wavelengths, Y, of 33.3 (1 mm), 100 (3 mm), 200 (6 mm), and 400 (12 mm) shows (Fig. 21) that the nonuniformity in the film thickness profile increases dramatically with the spanwise length of pressure variation. This is despite the fact that the magnitude of the pressure gradient is the same for all Cases. 50% variation in pressure gradient results in film thickness variation of less than 1% for 1 mm span and more than 15% for 1.2 cm span. The percentage variation in the rate of increase in the film thickness nonuniformity is maximum when Y is changed from 1 mm to 3 mm, and it decreases from 6 mm to 1.2 cm. This observation indicates that there is a critical wavelength at about 2 cm which corresponds to the maximum film thickness nonuniformity. The remaining issue is to explain the reason for this behavior.

Considering the y component of the Navier-Stokes Equation and noting that the length and velocity scale in the x-direction is small, that is $O(\delta)$, it is easy to show from order of magnitude analysis that the pressure gradient term is balanced mainly by

$$\partial p/\partial y \equiv \partial^2 v/\partial x^2$$

When we compute the RHS term from the computational results, we observe that its magnitude does not greatly vary between the Cases considered in this study. Therefore, the value of $\partial p/\partial y$ is also of the same order. This implies that as the wavelength of the pressure fluctuation

increases, the magnitude of the pressure gradient will increase. As we mentioned above, however, at a critical wavelength the value of the pressure gradient will approach a plateau with a further increase in Y.

Another important implication of the results of this study is the possibility of substrate deformation (i.e., the web and the rubber layer of the backing roll) resulting in coat-weight nonuniformities. Although substrate deformations are not considered in this work, the results of pressure profiles in Fig. 16 show great spanwise variations on the web under the blade. This could cause coat-weight nonuniformities due to nonuniform deformation of the web and the rubber layer as discussed by Pranckh and Scriven (1988) for a 2-D blade system.

Water absorption of the web is another important issue which is not considered in this work. The coating film with thickness variation just downstream of the blade perceives the following two effects, immobilization caused by dewatering and leveling by surface tension, then settles down to the final thickness as discussed by Bousfield (1991).

CONCLUSION

The present work is the first 3-D simulation to analyze the effect of pressure fluctuations upstream of the blade on coat-weight nonuniformities downstream of the blade. The primary result of this work is that the width of the domain, where pressure fluctuation is applied, greatly influences the magnitude of the film thickness variation for the parameters considered. In other words, a wider region of pressure fluctuation causes bigger coat-weight nonuniformities.

Although in this study we have not considered deformation and water absorption of the web and viscosity variation, the results provide important information regarding the large-scale streak patterns due to pressure fluctuations upstream of the blade.

ACKNOWLEDGEMENT

We gratefully acknowledge the Member Companies of the Institute of Paper Science and Technology and Mitsubishi Heavy Industries for supporting this work. Mr. John McKibben greatly assisted us in all aspects of computer simulations. Part of our research is conducted using the Cornell National Supercomputer Facility, a resource for the Center for Theory and Simulation in Science and Engineering at Cornell University, which is funded in part by the National Science Foundation, New York state, and the IBM Corporation.

NOTATION

Ca	Capillary number ($\equiv \mu W/\sigma$)
F	Cell fullness function
h	Blade gap
o	Magnitude of time step n to n + 1
p	Pressure
R	Reynolds number ($\equiv \rho Wh/\mu$)
R_1, R_2	Principle radii of curvature
t	Time
T	Period of pressure fluctuation

u_n	Fluid velocity normal to the interface
u_t	Fluid velocity tangent to the interface
u, v, w	Velocity components in the x, y, and z directions
υ^n	Velocity field at time step n
W	Coating speed
Y	Spanwise pressure fluctuation wavelength

Greek Letters

ν	Kinematic viscosity
μ	Dynamic viscosity
σ	Surface tension
τ	Blade thickness

LITERATURE CITED

Affes, H., A. T. Conlisk, and M. R. Foster, "The Steady Flow in a Short-Dwell Coater," Proc. TAPPI Coating Conference, TAPPI Press, Atlanta, GA, p. 299 (1990).

Aidun, C. K., "Fundamentals of Coating Systems," Report to Engineering Project Advisory Committee, The Institute of Paper Chemistry, (1989).

Aidun, C. K., "A Vortex-Free Short-Dwell Coater," to be published, TAPPI Coating Conference, (1992).

Aidun, C. K., N. G. Triantafillopoulos, and J. D. Benson, "Global Stability of a Lid-Driven Cavity with Throughflow: Flow Visualization Studies," *Phys. Fluid A*, **3,** 2081 (1991a).

Aidun, C. K., P. J. Veverka, and L. E. Scriven, "Onset of Air Entrainment: Mechanism," AIChE Annual Meeting, November 17-22, (1991b).

Benson, J. D. and C. K. Aidun, "Hot Film Anemometer Measurements of Unsteady Flow in a Lid-Driven Cavity," submitted for publication, (1991).

Bousfield, D. W., "The Leveling of Coating Defects," Proc. TAPPI Coating Conference, TAPPI Press, Atlanta, GA, p. 101 (1991).

Chen, K. S. A. and L. E. Scriven, "On the Physics of Liquid Penetration into a Deformable Porous Substrate," Proc. TAPPI Coating Conference, TAPPI Press, Atlanta, GA, p. 93 (1989).

Christodoulou, K. N. and L. E. Scriven, "The Fluid Mechanics of Slide Coating," *J. Fluid Mech.*, **208,** 321, (1989).

Conlisk, A. T. and M. R. Foster, "The Steady Flow in a Short-Dwell Coater II," Proc. TAPPI Coating Conference, TAPPI Press, Atlanta, GA, p. 327 (1991).

Freitas, C. J., R. L. Street, A. N. Findikakis, and J. R. Koseff, "Numerical Simulation of Three-Dimensional Flow in a Cavity," *International Journal for Numerical Methods in Fluid*, **5**, 561, (1985).

Hirt, C. W., B. D. Nicols, and N. C. Romero, "SOLA - A Numerical Solution Algorithm for Transient Fluid Flows," Los Alamos Report No. LA-5852 (1975).

Koseff, J. R. and R. L. Street, "The Lid-Driven Cavity Flow: A Synthesis of Qualitative and Quantitative Observations," *J. Fluids Eng.*, **106**, 390, (1984).

Leonard, B. P., "A Stable and Accurate Convective Modelling Procedure Based on Quadratic Upstream Interpolation," *Computer Methods in Applied Mechanics and Engineering*, **19**, 59, (1978).

Li, A., Personal Communication, (1990).

Li, A. and J. Burns, Personal Communication, (1991).

McKibben, J. F. and C. K. Aidun, "Computational Visualization of Three-Dimensional Free-Surface Flows," Proc. TAPPI Engineering Conference, TAPPI Press, Atlanta, GA, **2**, 711, (1991).

Michael, D. H., "The Separation of a Viscous Liquid at a Straight Edge," *Mathematika*, **5**, 82, (1958).

Pranckh, F. R. and L. E. Scriven, "The Physics of Blade Coating of Deformable Substrate," Proc. TAPPI Coating Conference, TAPPI Press, Atlanta, GA, p. 217, (1988).

Pranckh, F. R. and L. E. Scriven, "Elastohydrodynamics of Blade Coating," *AIChE J.*, **36**, 587, (1990).

Torrey, M. D., R. C. Mjolsness, and L. R. Stein, "NASA-VOF3D: A Three-Dimensional Computer Program for Incompressible Flows with Free Surfaces," Los Alamos Report No. LA-11009-MS (1987).

Triantafillopoulos, N. G. and C. K. Aidun, "Relation Between Flow Instability in Short-Dwell Ponds and Cross Directional Coat Weight Nonuniformities," *Tappi J.*, **73**, 127, (1990).

Triantafillopoulos, N. G., G. R. Rudemiller, and C. K. Aidun, "Fluid Dynamics of Short-Dwell Coater Pond Flows, Numerical Simulation," Int'l Symp. Coating Structures and Rheology, INSKO, Helsinki, Finland, (1989).

Triantafillopoulos, N. G., G. R. Rudemiller, T. Farrington Jr., and J. D. Lindsay, "Numerical Simulation of Short-Dwell Coater Pond Flows," Proc. TAPPI Coating Conference, TAPPI Press, Atlanta, GA, p. 209, (1988).

Yeverka, P. J. and C. K. Aidun, "Flow Visualization of Air Entrainment and Dynamic Contact Line Instability in Low-Speed Roll Coating," Proc. TAPPI Engineering Conference, TAPPI Press, Atlanta, GA, **2**, 719, (1991).

FIGURE CAPTIONS

Figure 1. Schematic of a short-dwell coater.

Figure 2. Sequence of transitions from (a) steady state to (b) time-periodic, (c) quasi-periodic, and (d) unsteady state in a cavity simulating the pond of a short-dwell coater.

Figure 3. Summary of mechanisms which may lead to wet streaks.

Figure 4. Illustration of the (a) blade geometry and the coordinate system and (b) two-dimensional cross section of the domain.

Figure 5. Illustration of the (a) coarse and the (b) fine grid systems for the two-dimensional computations (number inside the arrow indicates the number of cells).

Figure 6. Evolution of the free surface for (a) coarse and (b) fine grids.

Figure 7. Comparison of the free surface computations using the fine and the coarse grid systems.

Figure 8. The steady state film thickness profile with the increased domain length.

Figure 9. Illustration of the grid system for the two-dimensional case with temporal pressure fluctuation.

Figure 10. Variation in surface thickness due to pressure fluctuation at the blade entrance at Reynolds number, (A) R = 12, (B) R = 24, and (C) R = 36.

Figure 11. Film thickness deviation from the average value.

Figure 12. Illustration of the grid system and the free surface plot of the two-dimensional initial condition for the three-dimensional computation.

Figure 13. Pressure profile adjacent to the substrate (i.e., at x = 0).

Figure 14. Results from case 2 showing (a) film thickness profile downstream of the blade and (b) pressure profile under the blade.

Figure 15. Results from case 3 showing (a) film thickness profile downstream of the blade and (b) pressure profile under the blade.

Figure 16. Results from case 5 showing (a) film thickness profile downstream of the blade and (b) pressure profile under the blade.

Figure 17. Result from case 10 showing the film thickness profile downstream of the blade.

Figure 18. Comparison of the film thickness profile upstream of the blade from computations with 10 and 20 cells in the y-direction.

Figure 19. Comparison of pressure profile under the blade from computations with 10 and 20 cells in the y-direction.

Figure 20. Comparison of the film thickness profile upstream of the blade from computations using SOLA and QUICK Finite Difference Methods.

Figure 21. Comparison of the spanwise film thickness profile for pressure variations having wavelengths of 33.3 (1 mm), 100 (3 mm), 200 (6 mm), and 400 (12 mm).

Table 1. Velocity profile at three locations along the liquid film.

x	z = 17.25		z = 19.75		z = 24.75	
	$ux10^6$	w	$ux10^6$	w	$ux10^6$	w
.1	-5.5	0.9999	-2.0	0.99995	-0.05	1
.2	-20.5	0.9997	-8.0	0.99990	-0.05	1
.3	-44.5	0.9995	-30.5	0.99985	-0.35	1
.4	-74.5	0.9994	-45.5	0.99985	-0.45	1

Table 2. Boundary and flow parameters for the three-dimensional computation.

Parameter	Dimensionless	Dimensional
Speed of substrate, W	1	20 m/s
Blade gap, h	1	3×10^{-5} m
Blade thickness, τ	—	1×10^{-3} m
Density, ρ	—	1200 kg/m^3
Viscosity, μ	—	.05 pa.s
Surface tension, σ	—	.05 N/m
$\langle dp/dz \rangle$	1.44	-1.6×10^9 pa/m
R	14.4	—
Ca	20	—

Table 3. 3-D Cases (All of the Cases except 6, 7, and 8 use the QUICK method).

Case	CD-Span Length, Y	No. of Cells in CD	Inflow Pressure Fluctuation	Remarks
1	-	-	None	Base case (2-D SS)
2	33.3 (1 mm)	10	Full-wave	
3	100 (3 mm)	20	Full-wave	
4	100 (3 mm)	10	Full-wave	Same result as Case 3
5	200 (6 mm)	20	Full-wave	
6	33.3 (1 mm)	10	Full-wave	SOLA
7	100 (3 mm)	20	Full-wave	SOLA
8	200 (6 mm)	20	Full-wave	SOLA
9	100 (3 mm)	10	Half-wave	Equivalent to 6 mm Full-wave
10	200 (6 mm)	20	Half-wave	Equivalent to 12 mm Full-wave

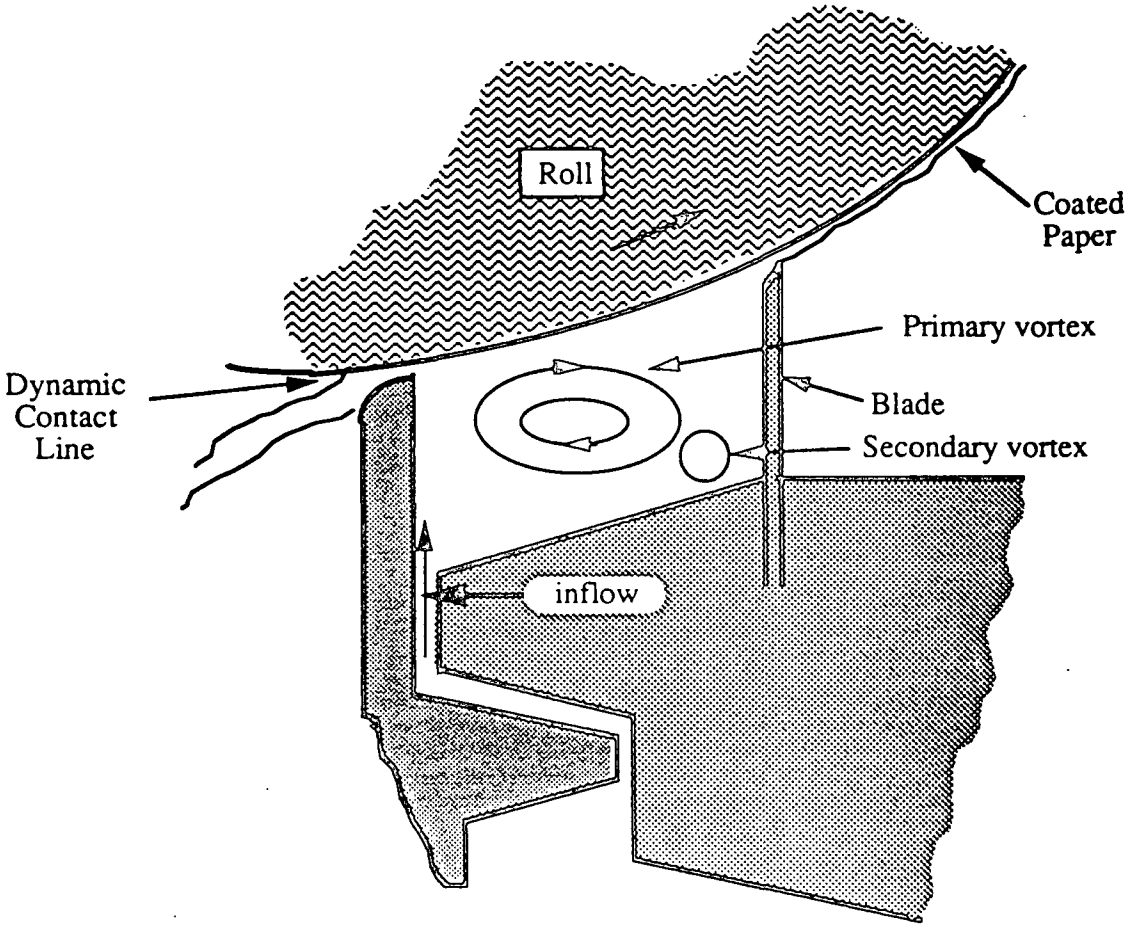

Figure. 1. Schematic of a short-dwell coater

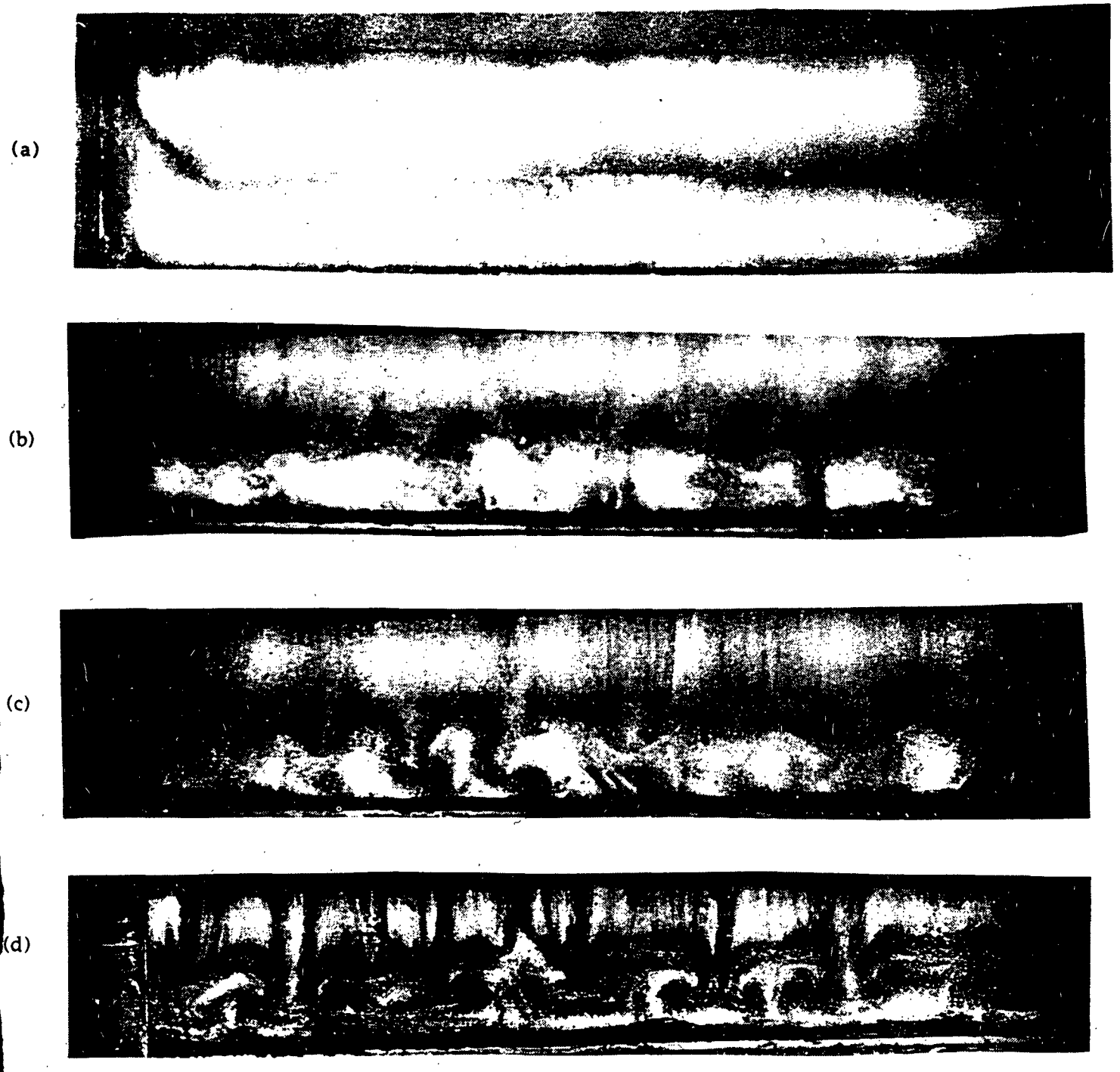

Figure 2. Sequence of transitions from (a) steady state to (b) time-periodic, (c) quasi-periodic, and (d) unsteady state in a cavity simulating the pond of a short-dwell coater.

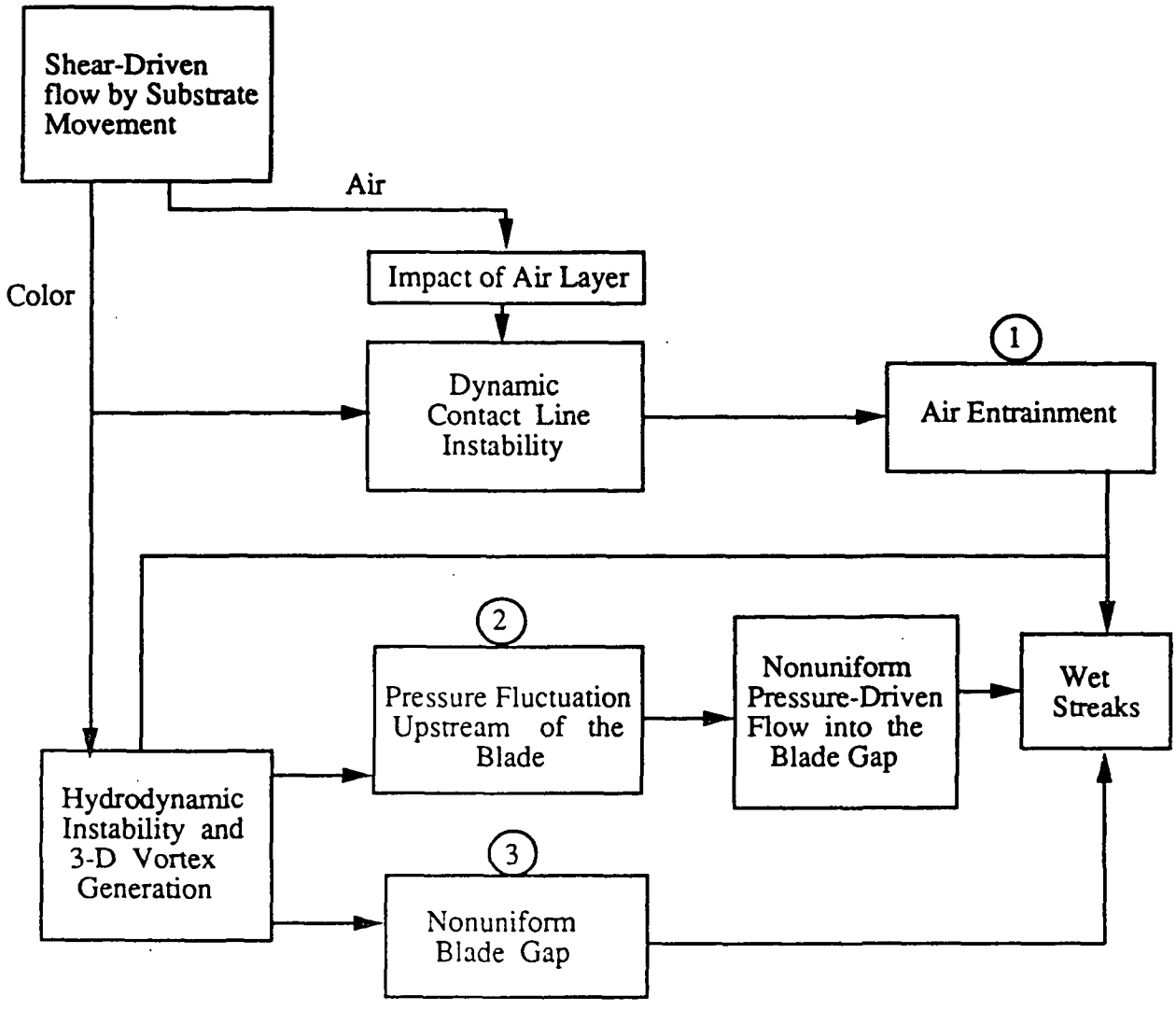

Figure 3. Summary of mechanisms which may lead to wet streaks.

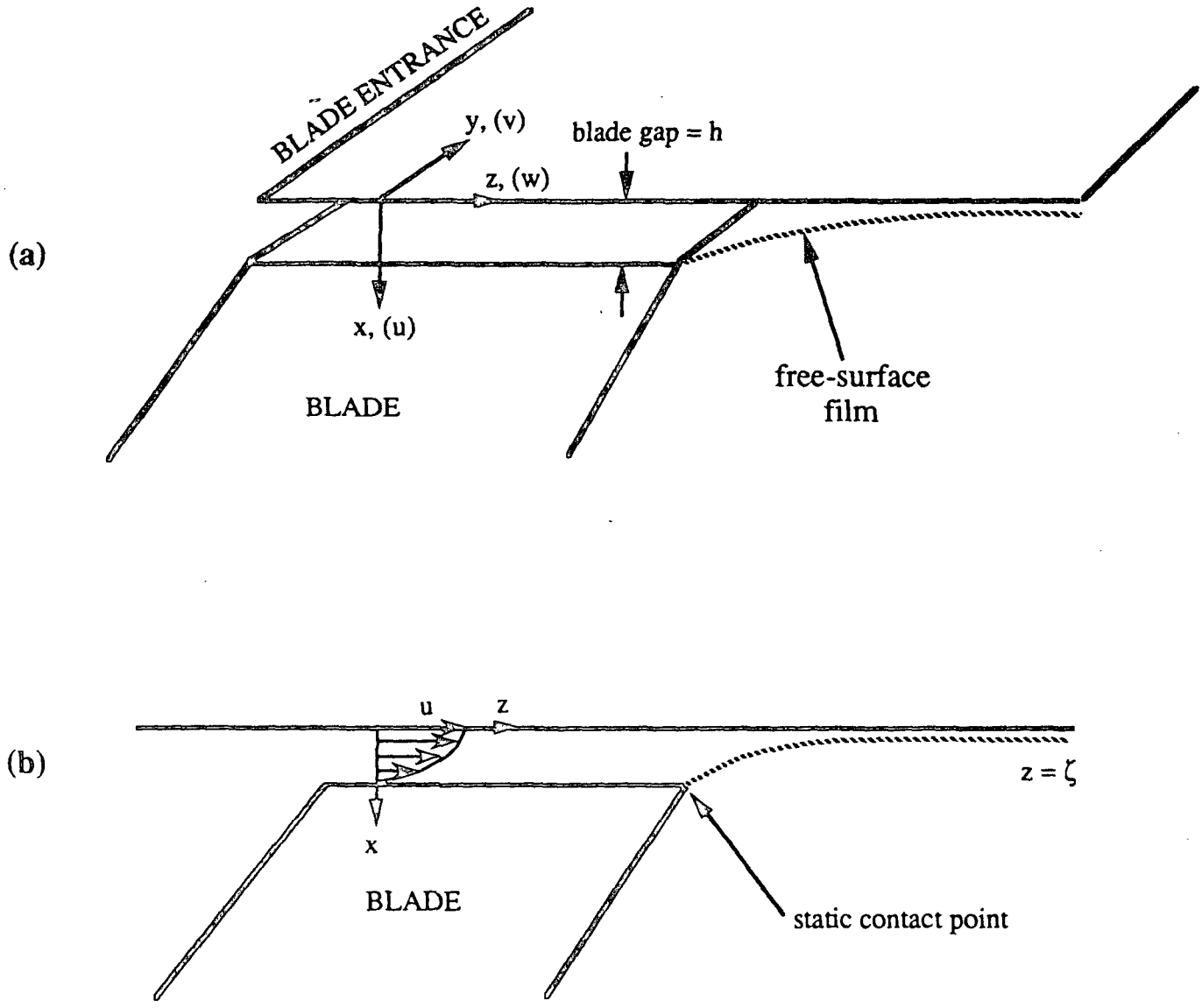

Figure 4. Illustration of the (a) blade geometry and the coordinate system and (b) two-dimensional cross section of the domain.

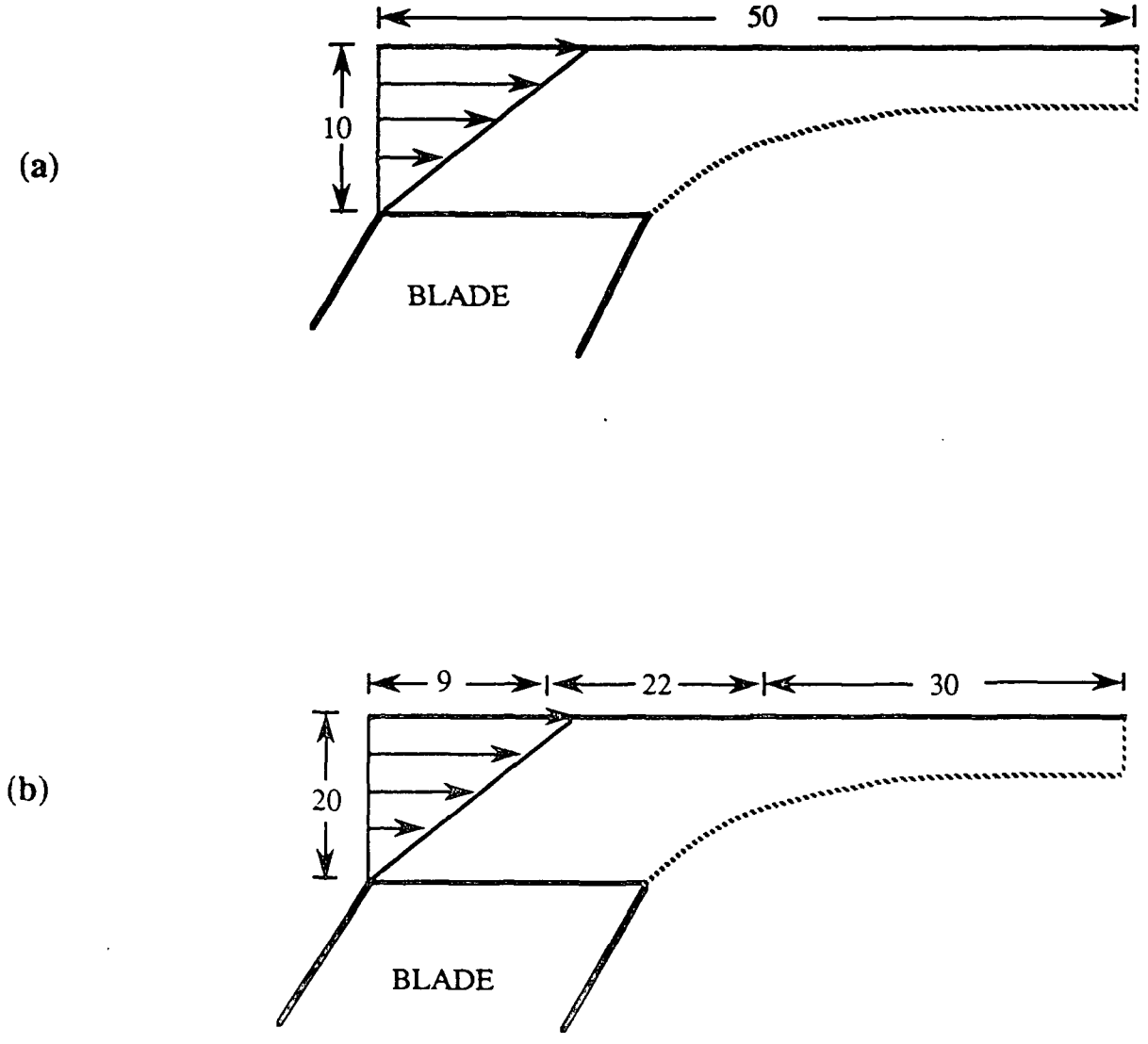

Figure 5. Illustration of the (a) coarse and the (b) fine grid systems for the two-dimensional computations (number inside the arrow indicates the number of cells).

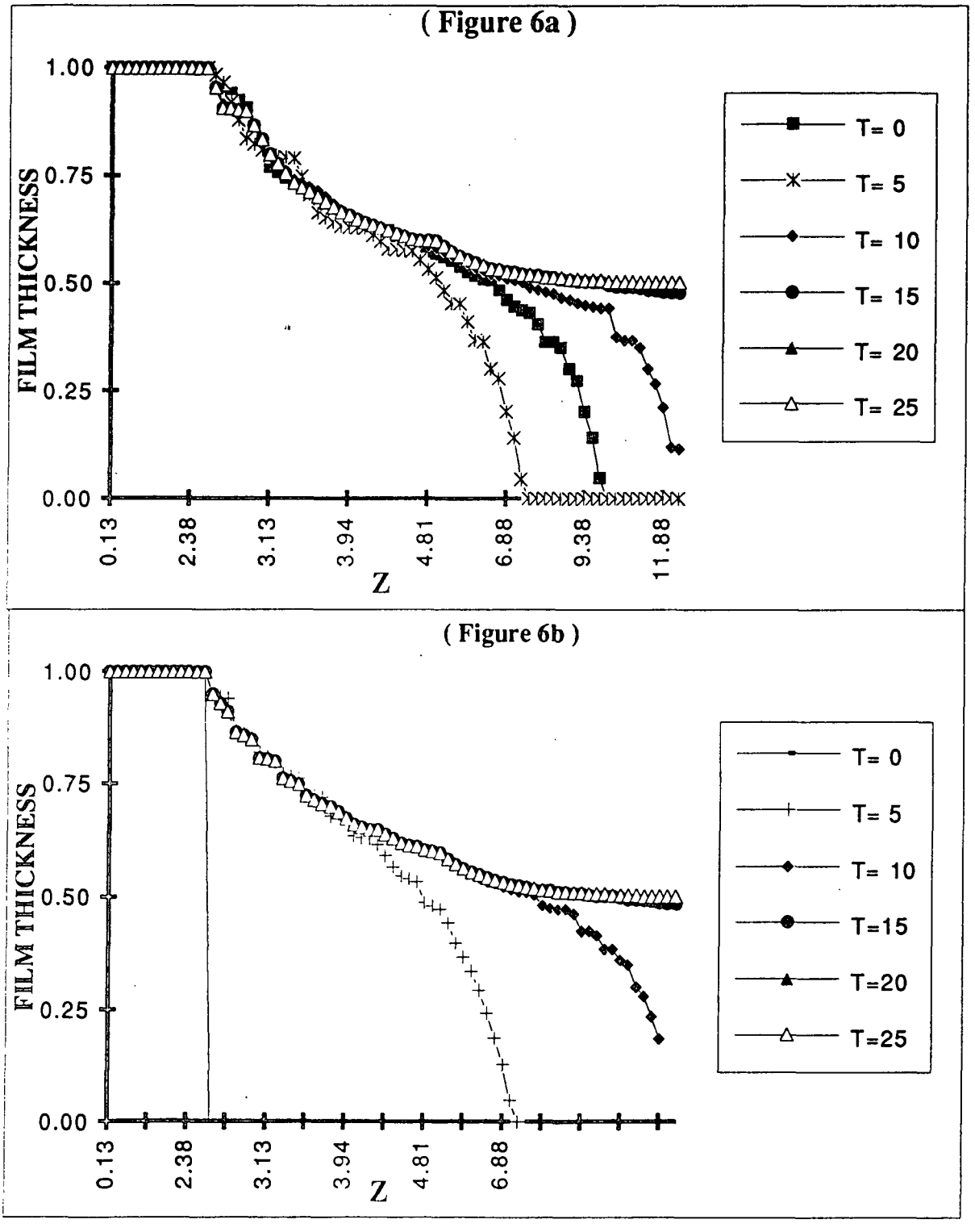

Figure 6. Evolution of the free surface for (a) coarse and (b) fine grids.

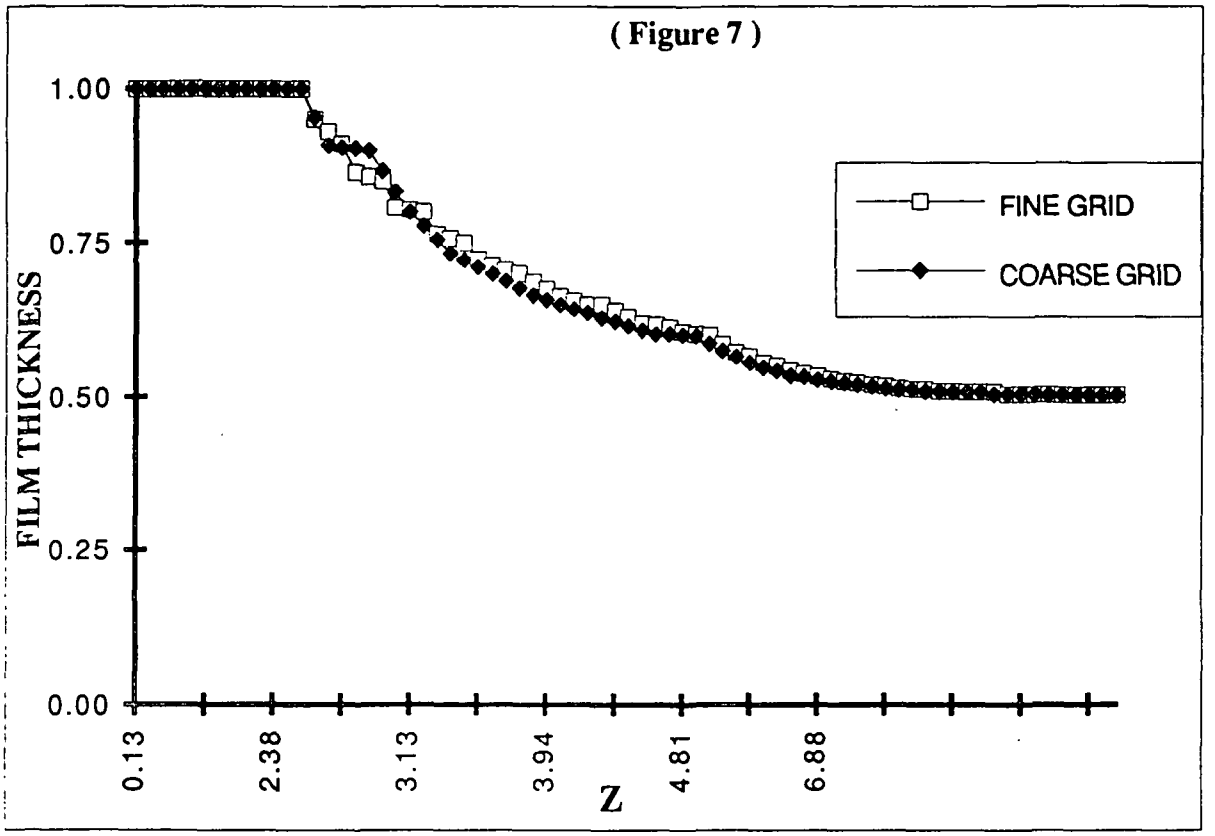

Figure 7. Comparison of the free surface computations using the fine and the coarse grid systems.

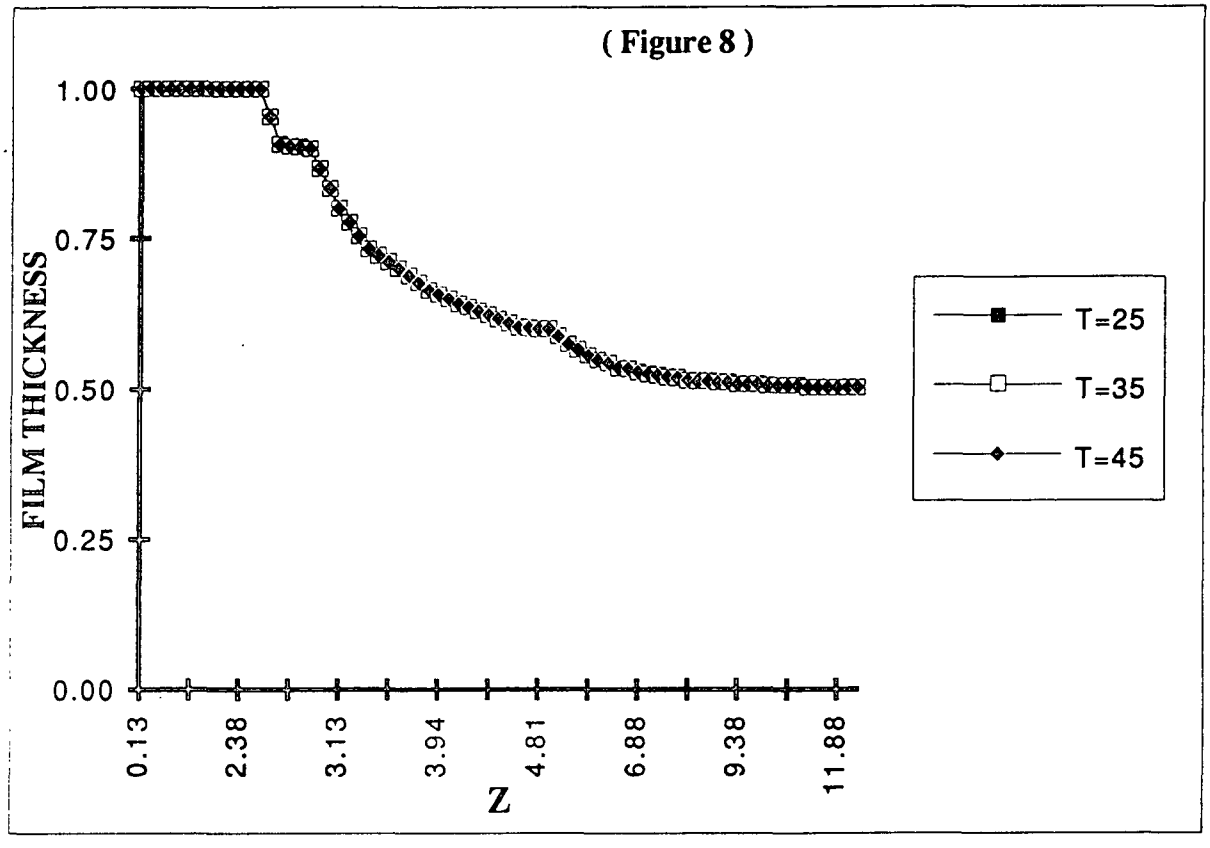

Figure 8. The steady state film thickness profile with the increased domain length.

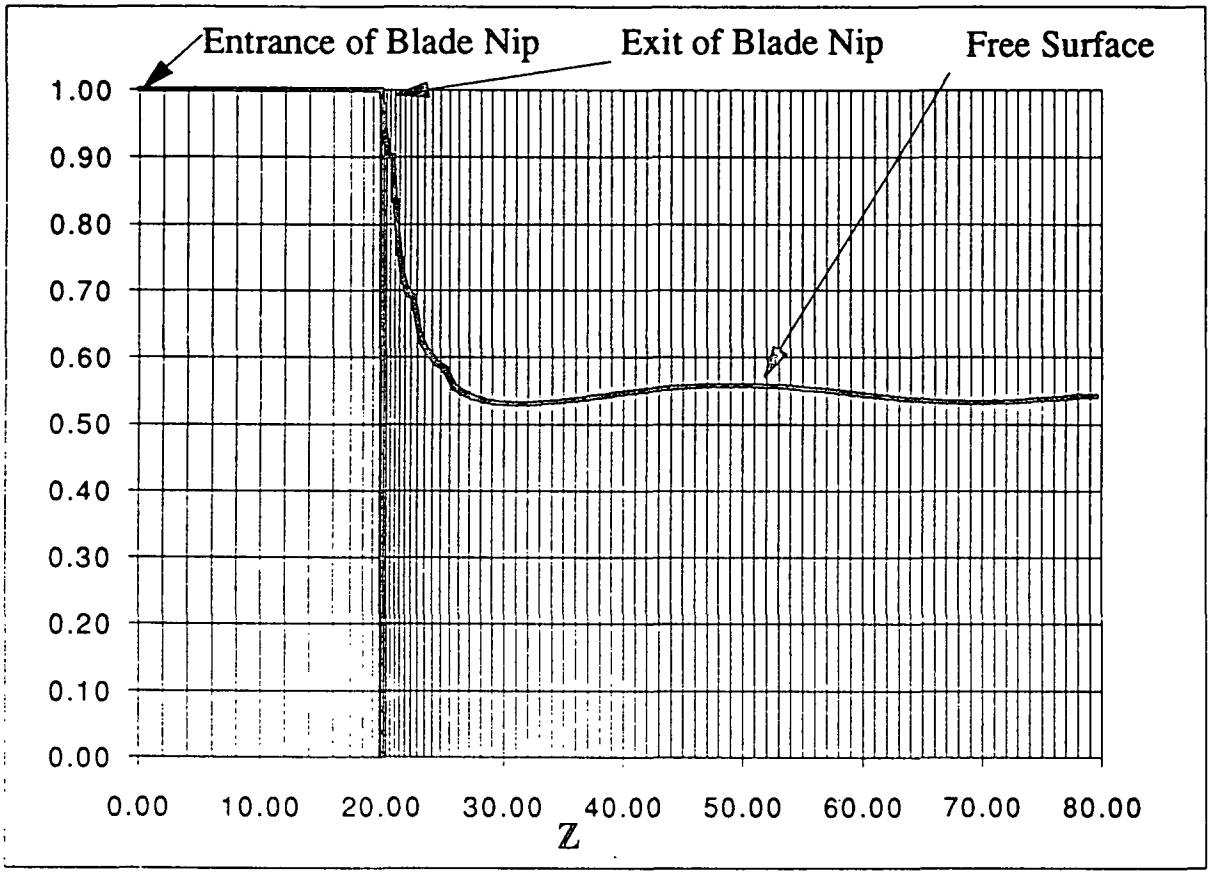

Figure 9. Illustration of the grid system for the two-dimensional case with temporal pressure fluctuation.

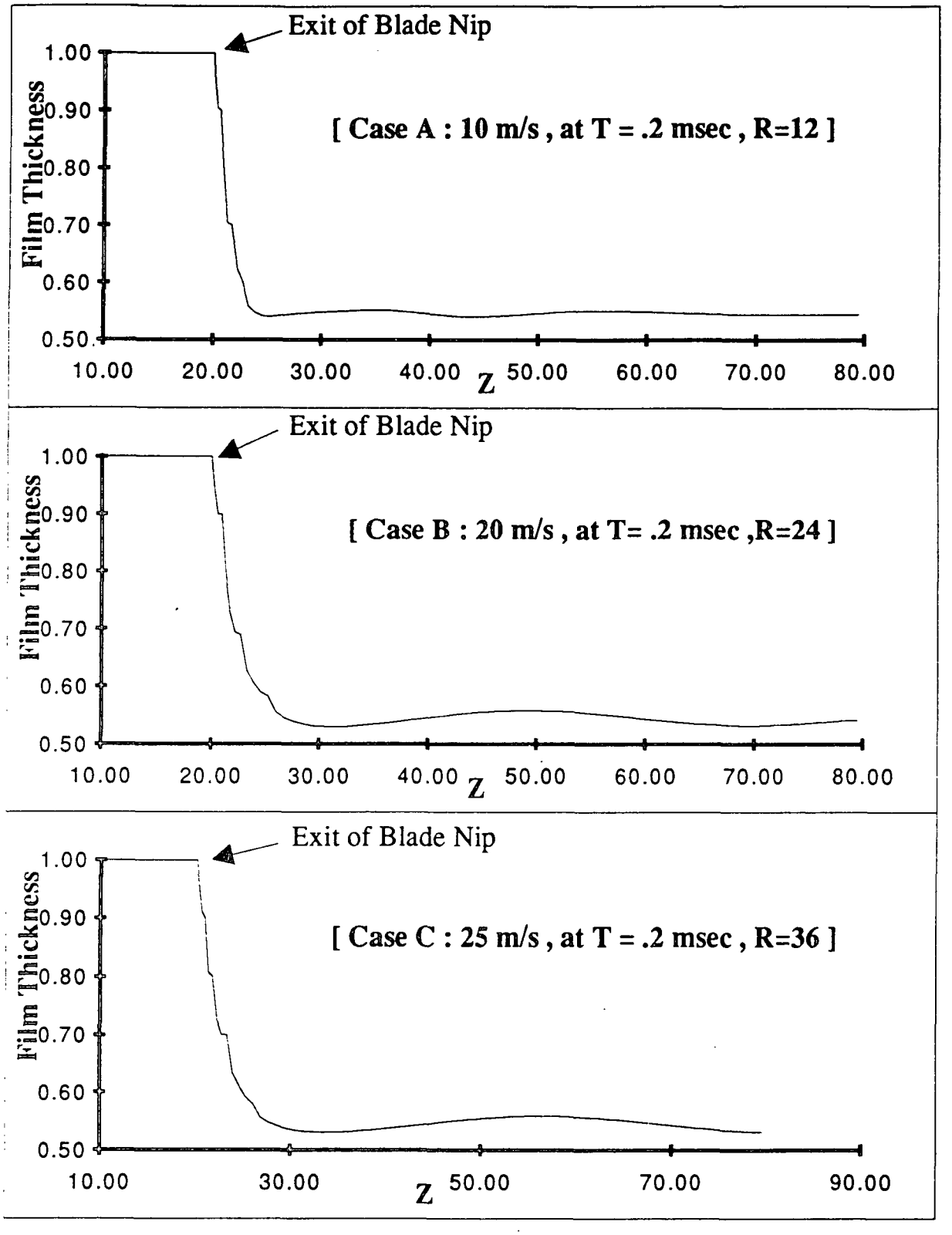

Figure 10. Variation in surface thickness due to pressure fluctuation at the blade entrance at Reynolds number, (A) R=12, (B) R=24, and (C) R=36.

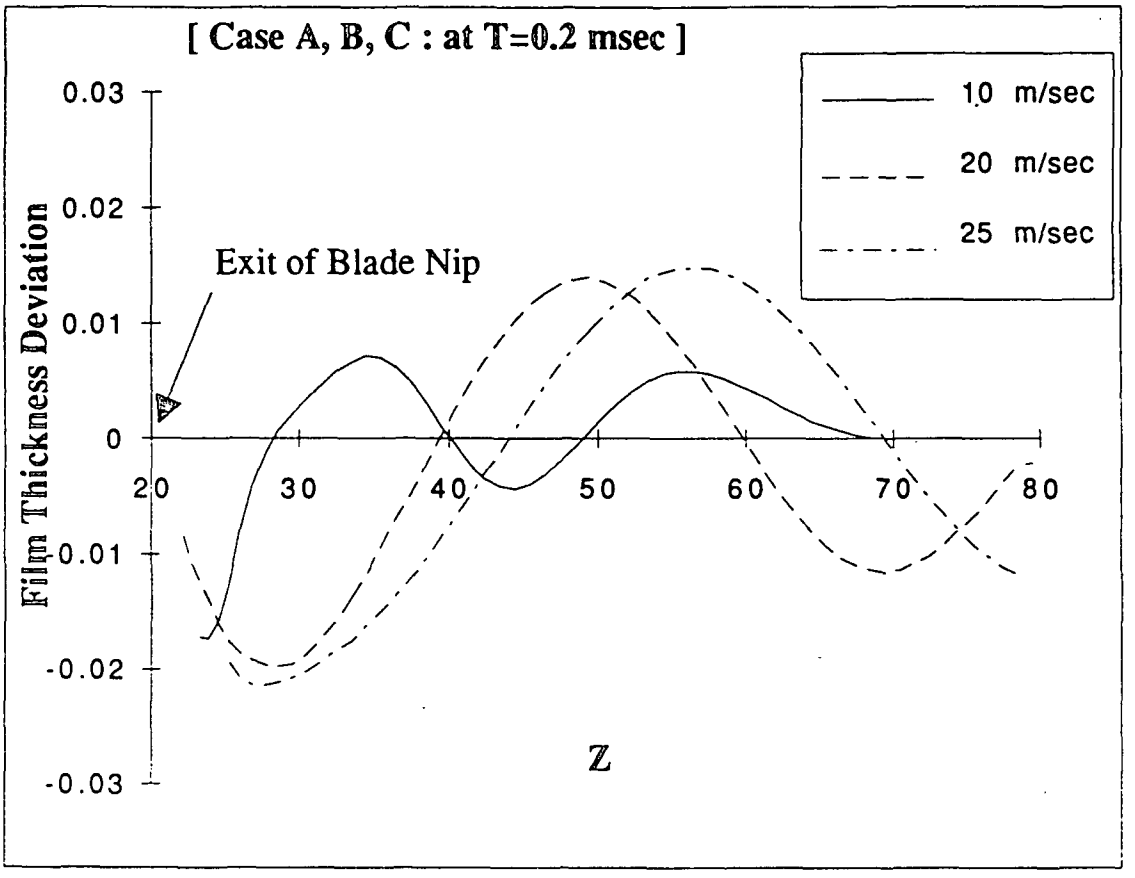

Figure 11. Film thickness deviation from the average value.

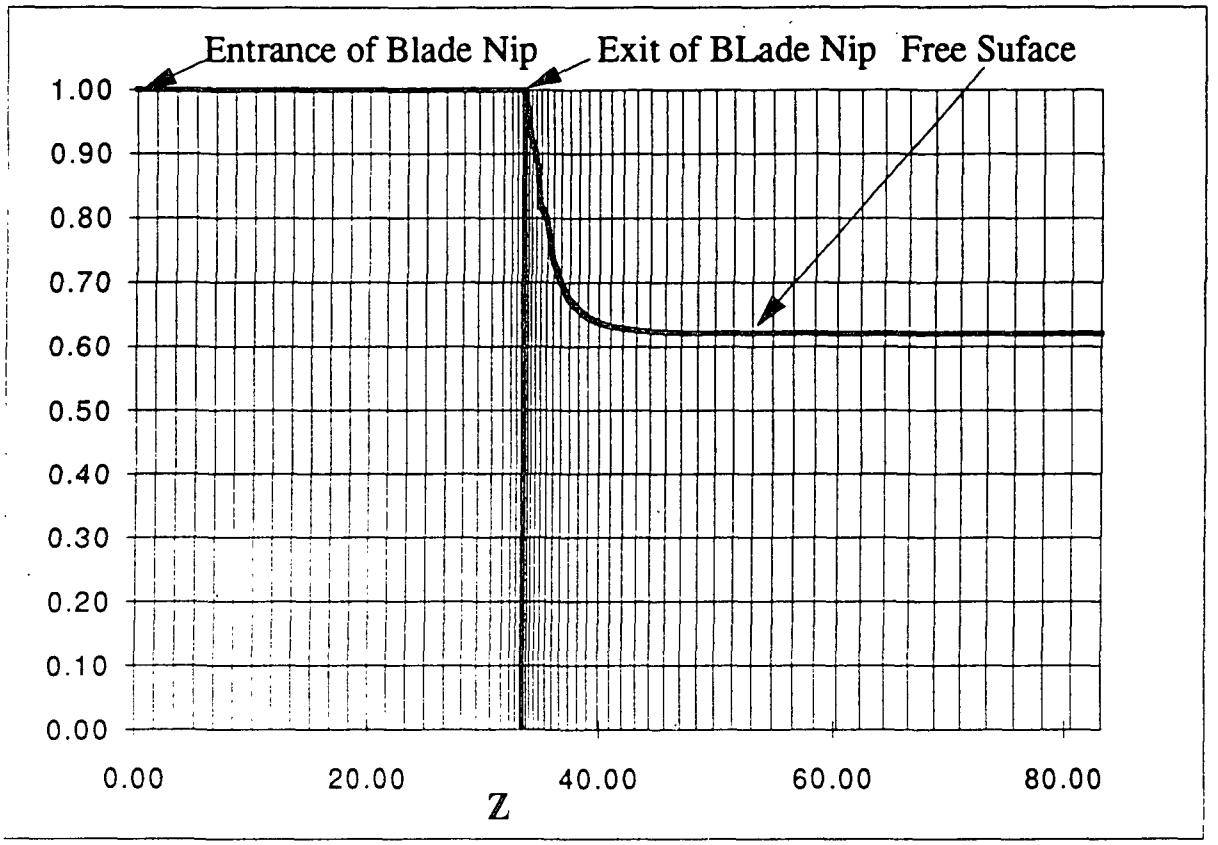

Figure 12. Illustration of the grid system and the free surface plot of the two-dimensional initial condition for the three-dimensional computation.

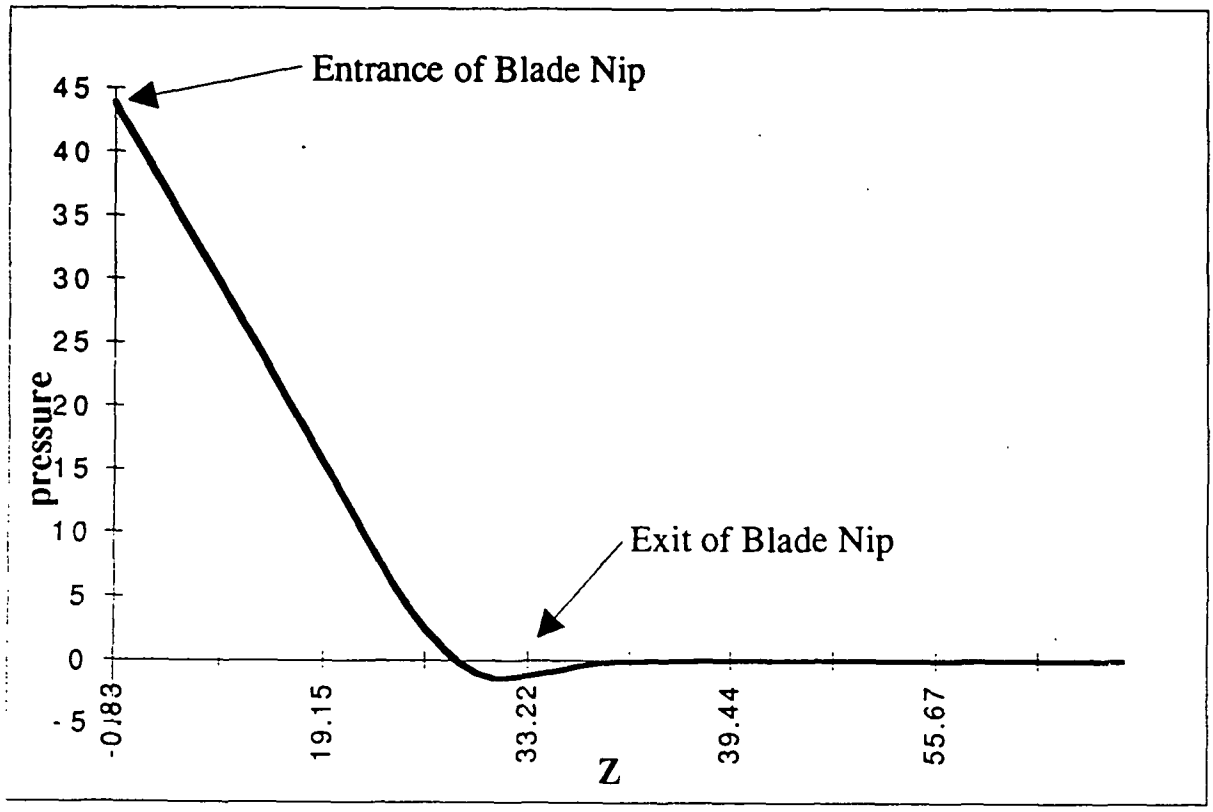

Figure 13. Pressure profile adjacent to the substrare (i.e., at x=0).

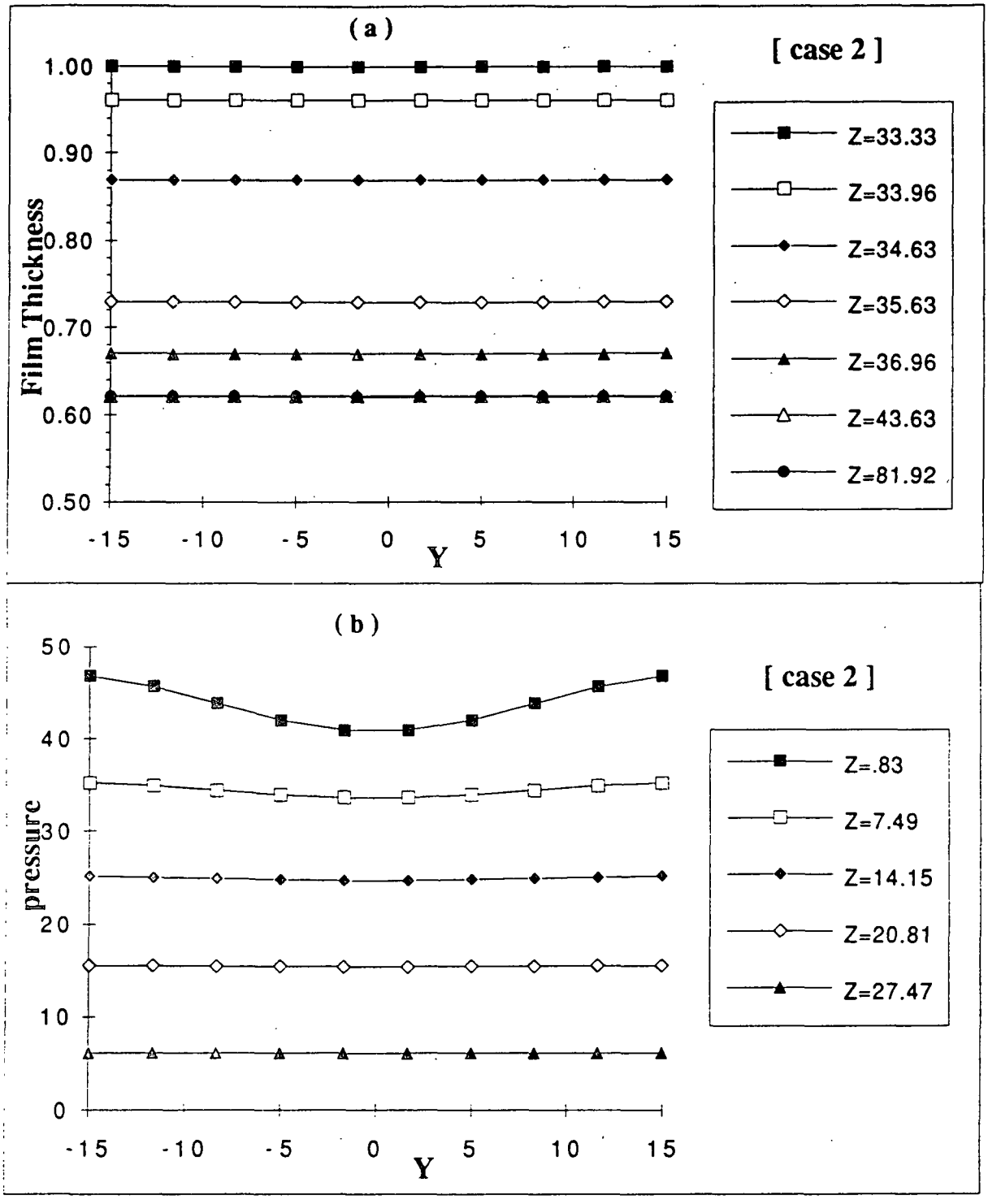

Figure 14. Results from case 2 showing (a) film thickness profile downstream of the blade and (b) pressure profile under the blade.

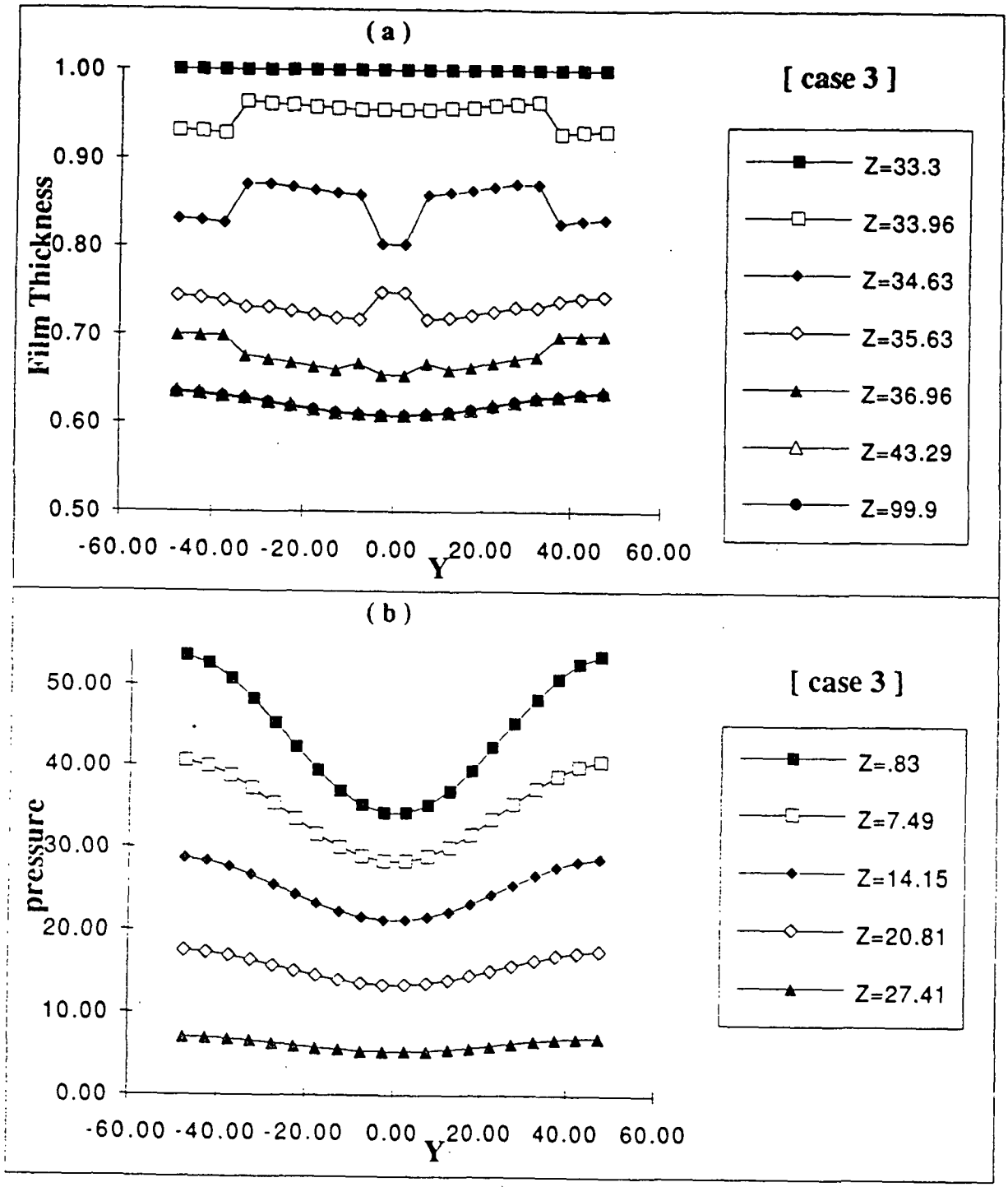

Figure 15. Results from case3 showing (a) film thickness profile downstream of the blade and (b) pressure profile under the blade.

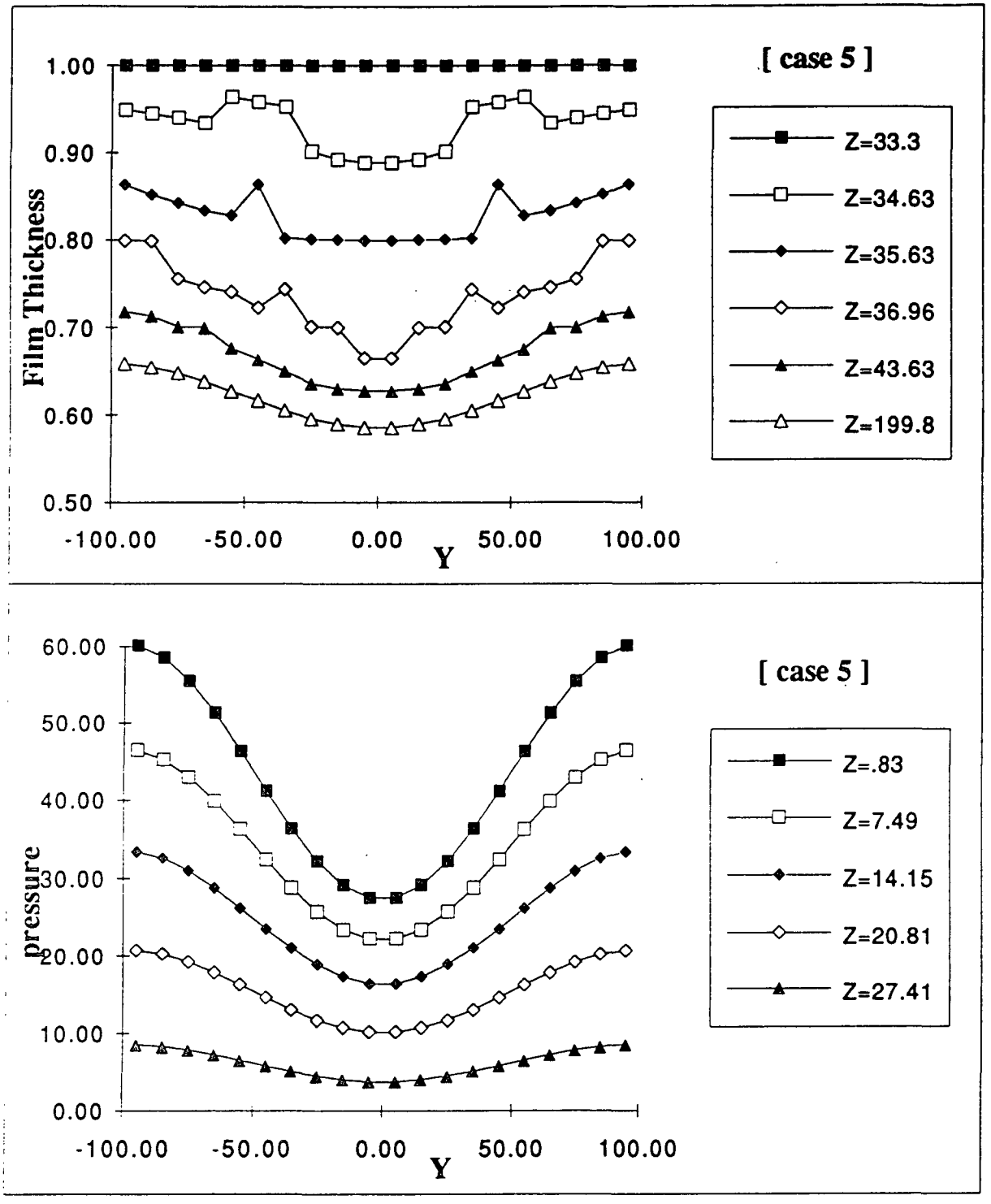

Figure 16. Results from case 5 showing (a) film thickness profile downstream of the blade and (b) pressure profile under the blade.

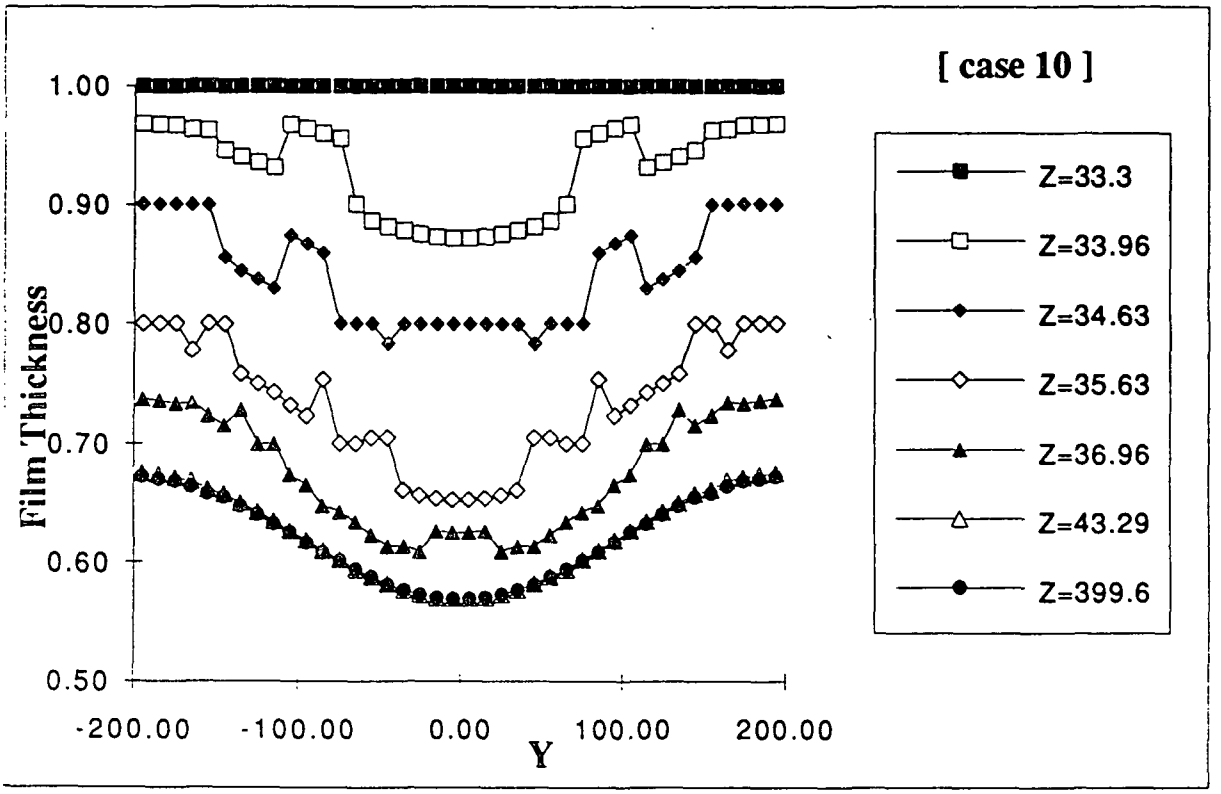

Figure 17. Result from case 10 showing the film thickness profile downstream of the blade.

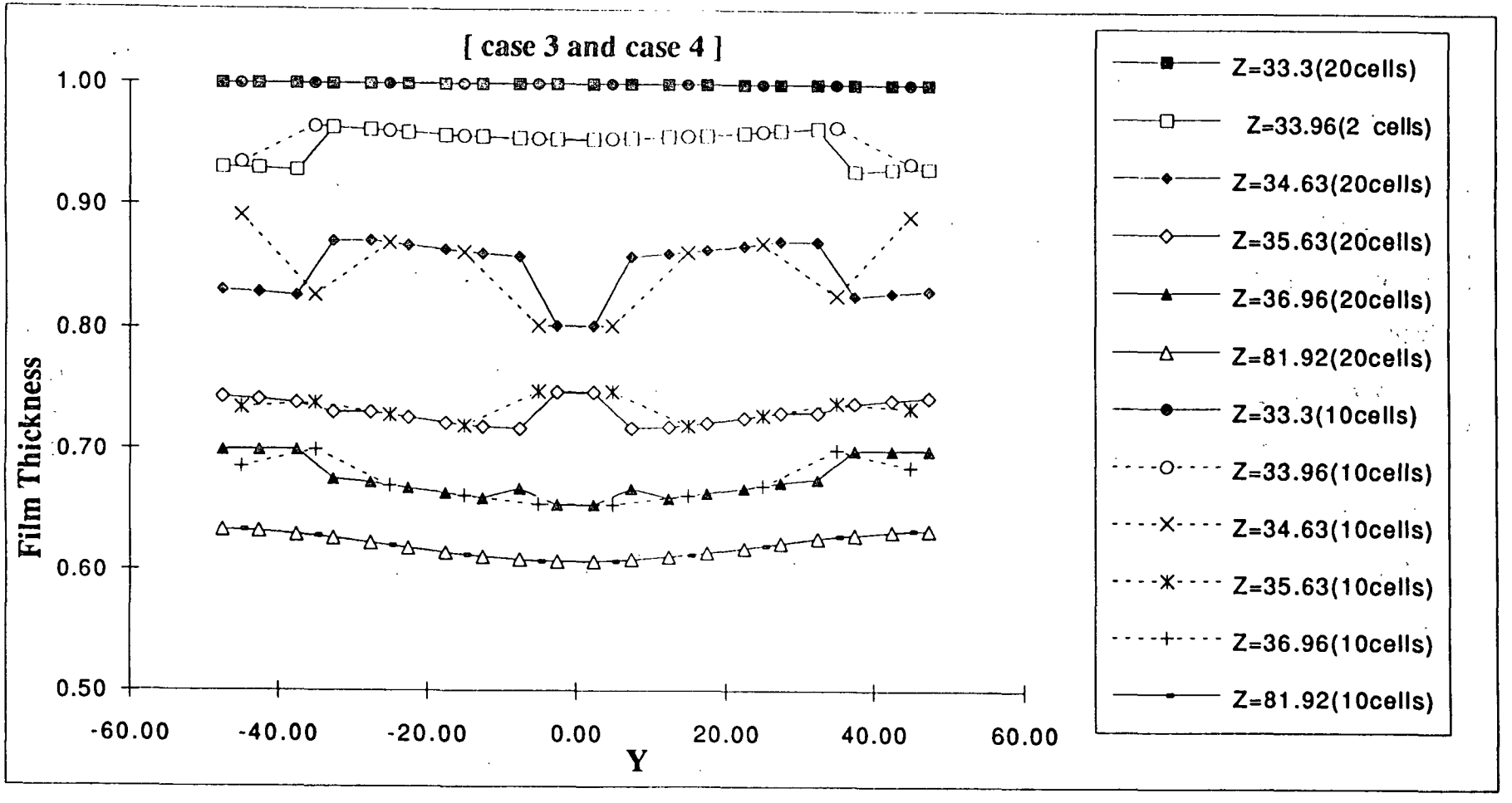

Figure 18. Comparison of the film thickness profile upstream of the blade from computations with 10 and 20 cells in the y direction.

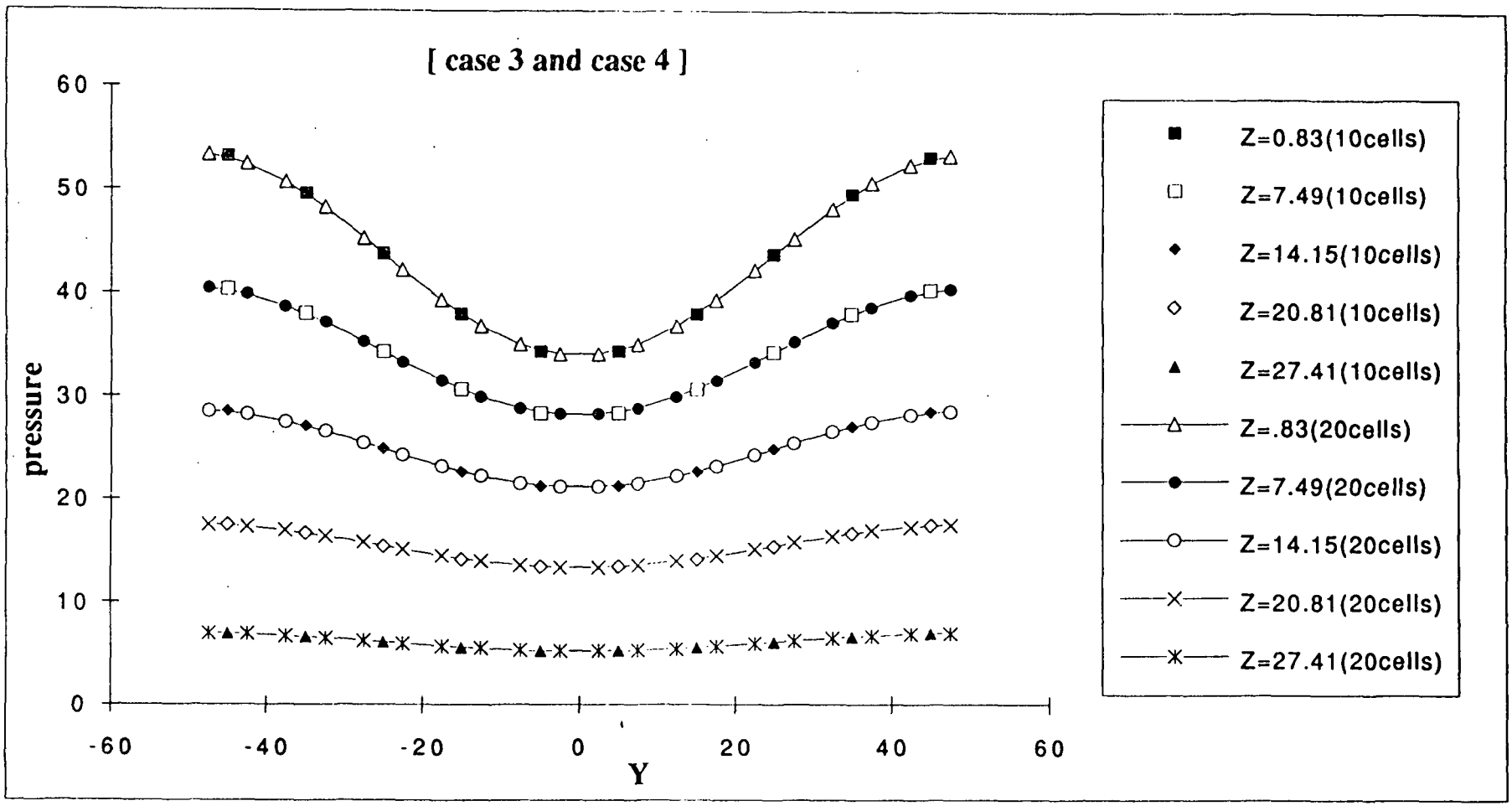

Figure 19. Comparison of pressure profile under the blade from computations with 10 and 20 cells in the y direction.

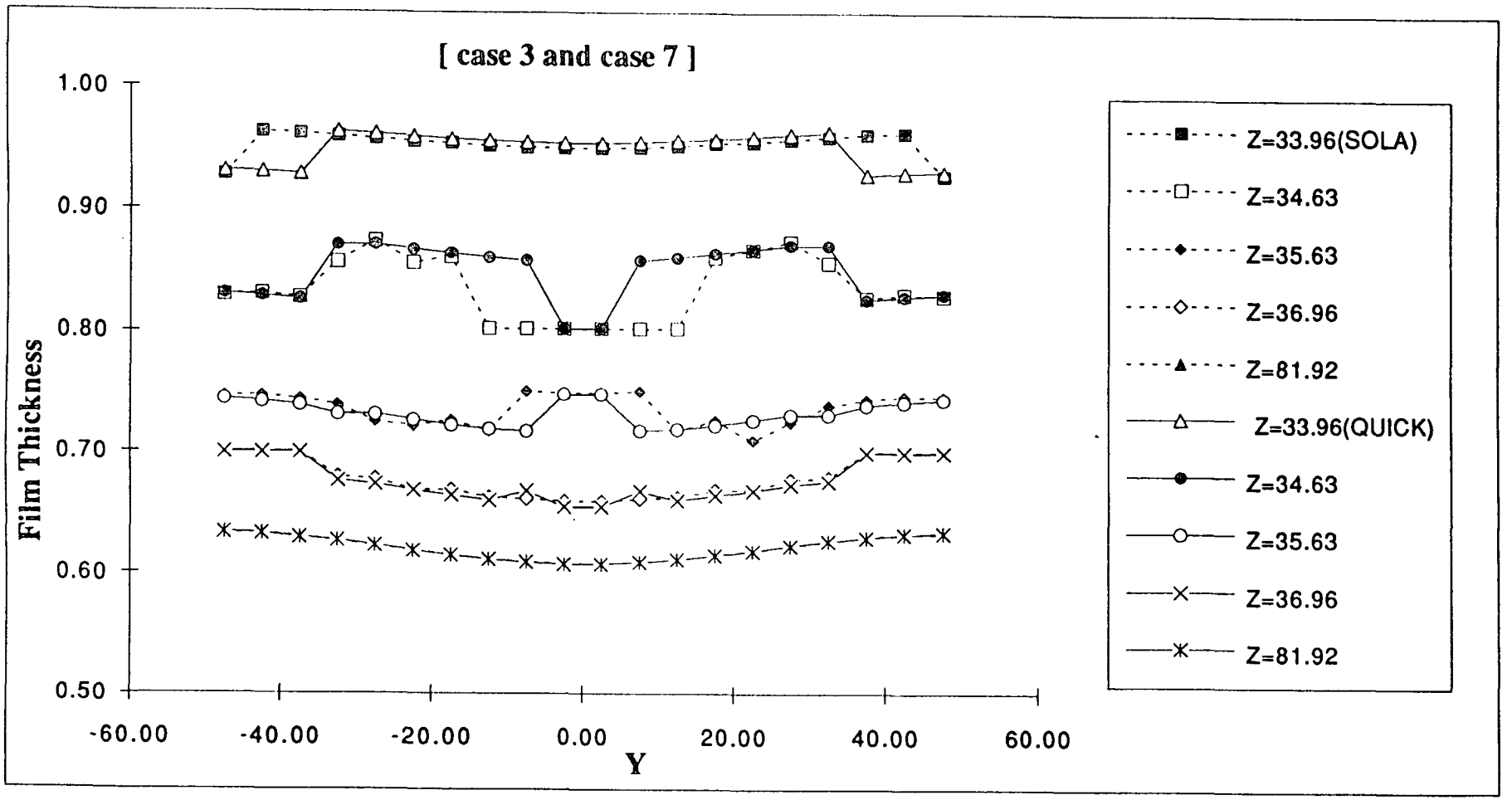

Figure 20. Comparison of the film thickness profile upstream of the blade from computations using SOLA and QUICK Finite Difference Methodes.

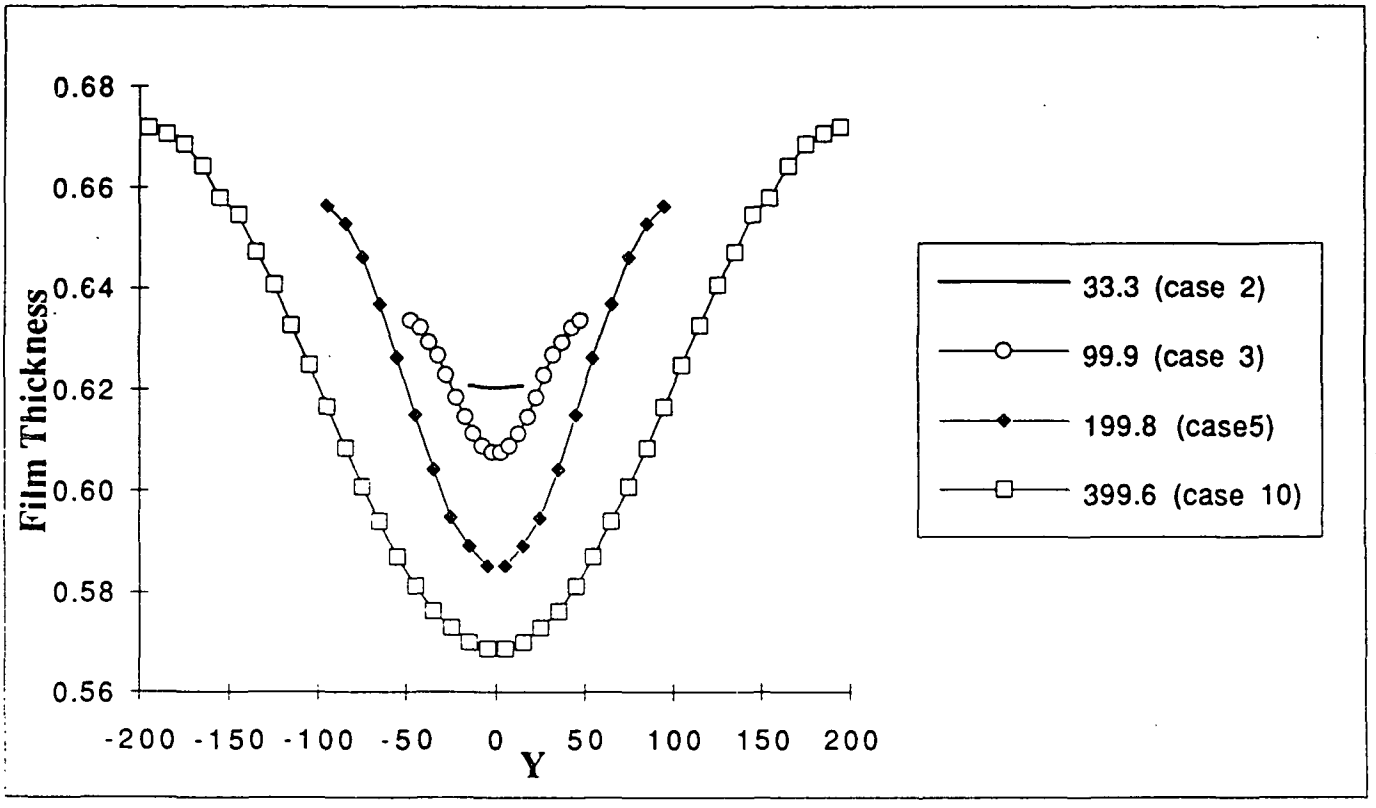

Figure 21. Comparision of the film thickness profile spanwise for pressure variations having wavelenghts of 33.3 (1 mm), 100 (3 mm), 200 (6 mm), and 400 (12 mm).